



The Gas Kinematics, Excitation, and Chemistry, in Connection with Star Formation, in Lenticular Galaxies

Olga K. Sil'chenko¹ , Alexei V. Moiseev^{1,2}, and Oleg V. Egorov^{1,2}

¹ Sternberg Astronomical Institute, M.V. Lomonosov Moscow State University, Universitetsky pr., 13, Moscow, 119234, Russia; olga@sai.msu.su, olgasil.astro@gmail.com, moisav@gmail.com, egorov@sai.msu.ru

² Special Astrophysical Observatory, Russian Academy of Sciences, Nizhnij Arkhyz, 369167, Russia
Received 2018 October 16; revised 2019 July 11; accepted 2019 July 20; published 2019 September 6

Abstract

We present long-slit and panoramic spectroscopy of extended gaseous disks in 18 S0 galaxies, mostly in groups. The gas has often decoupled kinematics: at least five galaxies demonstrate strongly inclined large-scale ionized gas disks, seven galaxies reveal circumnuclear polar disks, and in NGC 2551 the ionized gas, although confined to the main plane, counterrotates the stars. The gas excitation analysis reveals ionization by young stars in 12 of 18 S0 galaxies; current star formation in these galaxies is confined to ring-like zones coinciding with their UV rings. Gas oxygen abundances in the rings are around $0.7 Z_{\odot}$ and correlate neither with the ring radius nor with the metallicity of the stellar population. By applying tilted ring analysis to the velocity fields, we have traced the gas rotation plane lines of nodes along the radius. We find that current star formation proceeds usually where the gas lies strictly in the stellar disk planes and rotates circularly; the sense of the gas rotation does not matter (the counterrotating gas in NGC 2551 forms stars). In the galaxies without current star formation the extended gaseous disks either are in steady-state quasi-polar orientation or were acquired recently through the misaligned external filaments provoking shock-like excitation. Our data imply a crucial difference of the accretion regime in S0s with respect to spirals: the geometry of gas accretion in S0s is typically off-plane.

Key words: galaxies: elliptical and lenticular, cD – galaxies: evolution – galaxies: ISM – galaxies: kinematics and dynamics

1. Introduction

Lenticular galaxies were introduced as a distinct morphological type in the latest version of the “Hubble fork”—the galaxy morphology scheme by Hubble (1936); they were considered by Edwin Hubble as a transition type between ellipticals and spirals and *by definition* had large-scale stellar disks but lacked spiral arms and intense star formation. Since the global structures of lenticular and spiral galaxies were very similar (see, e.g., Laurikainen et al. 2010), and the only prominent difference was the red color of the disks and the absence of noticeable star formation regions within them, an idea had been formulated rather early that lenticular galaxies were former spirals devoid of gas (“*they show no trace of gas or anything of the sort*”; Baade 1975). However, further observations in the 21 cm line had shown that S0 galaxies could be rather rich in neutral hydrogen (see, e.g., van Driel & van Woerden 1991). The origin of this gas and reasons of the frequent absence of current star formation in the gas-rich S0s have remained unclear up to now.

Although lenticular galaxies typically have a lower ratio of cold gas mass to their luminosity than spiral galaxies (Knapp et al. 1985), it has been found that neutral and even molecular gas is present perhaps in most of them (Welch & Sage 2003; Sage & Welch 2006; Welch et al. 2010), though less than half of gas-rich S0 galaxies with extended cold gas disks experience current star formation of H II region type (Pogge & Eskridge 1993). The kinematics of ionized gas in S0s is often decoupled from that of their stellar disks, which had allowed Bertola et al. (1992) to conclude that at least 40% of emission-line S0s acquired their gas from some external sources rather recently. Later a factor of environment was found to be important: the studies by Davis et al. (2011) and Serra et al. (2012) showed that

among Virgo Cluster S0s the gaseous and stellar components revealed almost always strict kinematical alignment, while the non-Virgo S0s, those in groups and in the field, demonstrated decoupled gas kinematics in 50% of all cases. By following this logic, we have studied strongly isolated S0s that represent the extreme case of a sparse environment. We observed them with the long-slit spectrographs by aligning our slits with the photometric major axes (which are thought to trace the orientation of the stellar disk lines of nodes in the case of intrinsically round stellar disks). Our results (Katkov et al. 2014, 2015) have confirmed that without external forces to remove the gas, lenticular galaxies demonstrate extended ionized gas disks in more than 70% of all cases, and about half of them reveal gas counterrotation with respect to their stellar components. If the gas has been accreted by S0s from outside, such statistics implies that the directions of gas inflow are distributed isotropically. However, in the case of strongly isolated S0s the problem of searching for an external gas source (donors) remains unsolved.

Another interesting question that has intrigued us since then is the incidence of star formation in gas-rich S0s. In our sample of isolated S0s (Katkov et al. 2014, 2015) we found that both the gas ionized by young stars and the gas excited by shocks could be met in the disks, and it was not the amount of the gas that governed this dichotomy. By comparing the projections of the gas and star rotation velocities onto the line of sight along the spectrograph slit (aligned with the stellar disk major axis), we have suspected that star formation proceeds when the gas lies strictly in the planes of stellar disks, independently of the gas spin direction—coincident with the stellar component spin or antiparallel to it. However, we cannot determine exactly the orientation of the gas rotation plane by observing it only with the long slit; panoramic spectroscopy is needed. In this paper we just present the

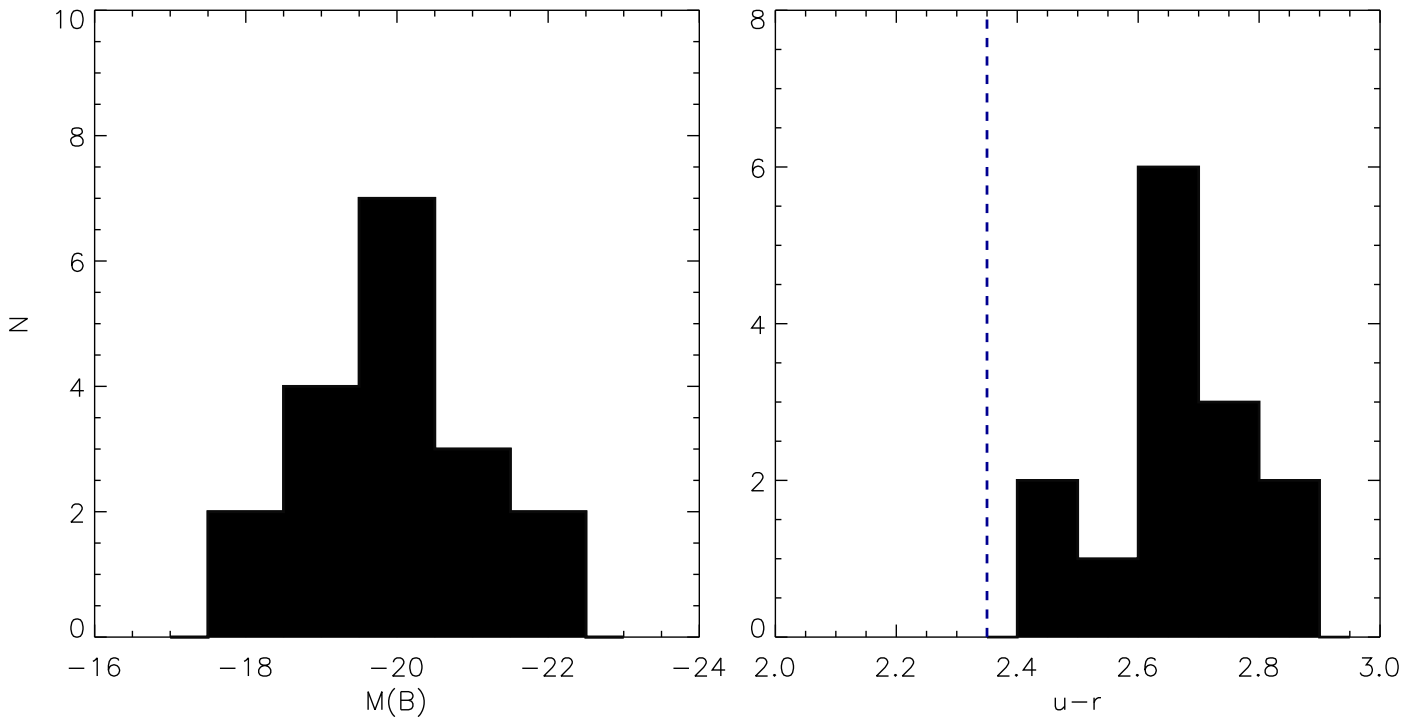


Figure 1. Properties of the sample: the distributions over integrated absolute magnitude assembled from the HyperLEDA (left) and over integrated $(u - r)_0$ color taken from the SDSS/DR9 (right). In the right panel we have also shown the boundary separating the red sequence and the blue cloud (Mateus et al. 2006) by the vertical dashed line.

results of our complex study of the ionized gas in 18 S0s for which we have undertaken both long-slit spectroscopy and velocity mapping with the scanning Fabry–Perot interferometer (FPI) by using the facilities of the Russian 6 m telescope of the Special Astrophysical Observatory of the Russian Academy of Sciences (SAO RAS).

2. Sample

The sample includes 18 S0 and S0/a galaxies with rather extended gaseous disks detected in optical-band emission lines; the presence of such disks either is known from our previous works (e.g., Sil'chenko et al. 2009; Ilyina et al. 2014; Proshina et al. 2019) or is suspected from the extended UV signal reported in Gil de Paz et al. (2007). To select the targets suitable to be studied with the scanning FPI, we have first undertaken long-slit spectroscopy to trace emission lines toward their full extension, and so our sample of nearby S0s is biased toward gas-rich objects. The sample is not representative over either galaxy characteristic; it is not volume or magnitude limited. However, the absolute magnitude range of the galaxies under consideration covers the full range of S0 luminosities, which is from $M_B = -18$ to $M_B = -22$ according to van den Bergh (2009) (Figure 1, left), and the galaxies are homogeneously red, belonging all to the red sequence (Figure 1, right). The list of their integrated properties assembled over the literature is given in Table 1. The majority of our galaxies, 13 of 18, demonstrate rings of various size, including those seen in the far-UV (FUV), according to the *GALEX* data, hence betraying possible recent star formation. Interestingly, our ringed S0s are mostly unbarred.

3. Observations

3.1. Long-slit Spectroscopy

Our long-slit spectral observations were made with the multi-mode focal reducer SCORPIO (Afanasiev & Moiseev 2005) and its improved version SCORPIO-2 (Afanasiev & Moiseev 2011) installed at the prime focus of the SAO RAS 6 m telescope. Both devices have the same slit size (6'1 in length and 1'' in width) with a scale along the slit of $0''.36 \text{ pixel}^{-1}$, while for a similar spectral resolution SCOPRIO-2 provides a twice as large spectral range. With the SCOPRIO-2 we exposed the full optical spectral range, namely, 3700–7200 Å, by using the volume-phase holographic grating VPHG1200@540, providing a spectral resolution of about 5 Å, whereas with SCORPIO we probed separately the narrower spectral ranges, 4800–5500 Å, 6200–7200 Å, or 5700–7500 Å, with the gratings VPHG2300G, VPHG1800R, and VPHG1200R, providing a resolution of about 2, 2.5, and 5 Å, respectively. The log of the observations is presented in Table 2, and the positions of the spectrograph slit against the galaxy images are shown in Figure 4.

The data were reduced in a standard way using the IDL software package developed in SAO RAS. It is at the edges of the slit that we derived the sky background to subtract it from the galaxy spectra, by applying the linear or polynomial (with a degree of 2–3) fit of the sky background distribution along the slit at every wavelength. Inhomogeneities of the optics transmittance and variations of the spectral resolution along the slit were taken into account by using the high signal-to-noise ratio (S/N) acquisitions of the twilight spectra. The stellar kinematics was analyzed by cross-correlating binned spectra with spectra of K-giant stars observed on the same nights as the galaxies; the description of this technique and references on the original papers are presented in our previous

Table 1
Global Parameters of the Galaxies

| Name | Type (NED ^a) | M_B (LEDA ^b) | M_H (NED) | $(g-r)$ (SDSS/DR9) | R_{25} (arcsec) (LEDA) | Environment ^c (NED) | $M_{H I}$ ($10^8 M_\odot$) (EDD ^d) | M_{H_2} ($10^8 M_\odot$) (Young et al. 2011) |
|-----------|-----------------------------|-------------------------------|----------------|------------------------|-----------------------------|-----------------------------------|---|---|
| IC 5285 | S0/a ^b | -21.97 | -24.32 | 0.84 | 39.5 | 4 | 37.5 | ... |
| NGC 252 | (R)SA(r)0+: | -21.42 | -25.13 | 0.78 | 49 | 4 | 28 | 6.29 (10) |
| NGC 774 | S0 | -20.17 | -23.69 | 0.86 | 39 | 4 | ... | ... |
| NGC 2551 | SA(s)0/a | -20.04 | -23.02 | $1.04(=(B-V)_{e,0}^2)$ | 47.5 | 4 | 12 | ... |
| NGC 2655 | SAB(s)0/a | -21.22 | -24.26 | $0.89(=(B-V)_{e,0}^2)$ | 117 | 4 | 11.4 | 1.3 (1) |
| NGC 2697 | SA(s)0+: | -18.66 | -22.26 | 0.72 (2) | 49 | 3 | 5.9 | 1.8 |
| NGC 2787 | SB(r)0+ | -18.45 | -23.34 | $0.95(=(B-V)_{e,0}^2)$ | 97 | 5 | 9.8 (3) | 0.18 (4) |
| NGC 2962 | (R)SAB(rs)0+ | -20.08 | -23.64 | 0.87 | 69 | 4 | 11.0 | <0.7 |
| NGC 3106 | S0 | -21.70 | -24.62 | 0.73 | 27 | 4 | 108 (5) | |
| NGC 3166 | SAB(rs)0/a | -20.30 | -24.34 | 0.81 | 134 | 4 | 4.5 (3) | 1.7 (6) |
| NGC 3182 | SA(r)0/a ^b | -19.81 | -22.84 | 0.77 | 57 | 4 | 0.08 (7) | 2.14 |
| NGC 3414 | S0pec | -20.03 | -23.39 | 0.76 | 81 | 4 | 1.9 (7) | <0.15 |
| NGC 3619 | (R)SA(s)0+: | -19.63 | -23.57 | 0.86 | 117 | 2 | 10.0 (7) | 1.9 |
| NGC 4026 | S0 | -19.11 | -23.16 | 0.80 | 131 | 2 | 3.2 (7) | 0.88 (3) |
| NGC 4324 | SA(r)0+ | -19.12 | -23.43 | 0.76 | 88.5 | 1 | 16.8 | 0.5 |
| NGC 7280 | SAB(r)0+ | -18.84 | -22.41 | 0.74 | 60 | 4 | 0.83 (7) | <0.3 |
| UGC 9519 | S0 ^b | -18.09 | -21.49 | 0.82 | 24 | 3 | 18.6 (7) | 5.9 |
| UGC 12840 | (R)SAB(s)0 ⁰ | -21.15 | -24.14 | 0.76 | 36 | 5 | 55 (8) | 6.2 (9) |

Notes.^a NASA/IPAC Extragalactic Database, <http://ned.ipac.caltech.edu>.^b Lyon-Meudon Extragalactic Database, <http://leda.univ-lyon1.fr>.^c Environments: 1—cluster member; 2—rich-group member; 3—loose-group member; 4—loose-group center; 5—field.^d Extragalactic Distance Database, <http://edd.ifa.hawaii.edu>.**References.** (1) Ueda et al. 2014; (2) Proshina et al. 2019; (3) Roberts et al. 1991; (4) Welch & Sage 2003; (5) Eder et al. 1991; (6) Wiklind & Henkel 1989; (7) Serra et al. 2012; (8) Haynes et al. 2011; (9) Lisenfeld et al. 2011; (10) O'Sullivan et al. 2018.

Table 2
SCORPIO/SCORPIO-2 Long-slit Spectroscopy of the Sample Galaxies

| Galaxy | Date | Grism | Sp. Range (Å) | Exposure (s) | PA(slit) (deg) | Seeing (arcsec) |
|-----------|-------------|--------------|---------------|-------------------|----------------|-----------------|
| IC 5285 | 2015 Oct 04 | VPHG1200R | 5700–7500 | 3 × 900 | 93 | 1.3 |
| NGC 252 | 2011 Nov 19 | VPHG1200@540 | 3700–7200 | 6 × 900 | 82 | 1.5 |
| NGC 774 | 2015 Oct 08 | VPHG2300G | 4800–5500 | 6 × 1200 | 170 | 3.6 |
| NGC 2551 | 2014 Dec 14 | VPHG1200@540 | 3700–7200 | 8 × 900 | 13 | 1.5 |
| NGC 2551 | 2015 Oct 06 | VPHG1200R | 5700–7500 | 3 × 900 | 55 | 2.6 |
| NGC 2655 | 2014 Dec 15 | VPHG1200@540 | 3700–7200 | 2 × 900 + 6 × 600 | 0 | 1.3 |
| NGC 2655 | 2014 Dec 15 | VPHG1200@540 | 3700–7200 | 3 × 600 + 8 × 450 | 102 | 1.3 |
| NGC 2787 | 2009 Mar 30 | VPHG2300G | 4800–5500 | 4 × 1800 | 109 | 1.5 |
| NGC 2787 | 2009 Mar 30 | VPHG2300G | 4800–5500 | 3 × 1200 + 661 | 72 | 1.5 |
| NGC 2787 | 2012 Apr 14 | VPHG1200@540 | 3700–7200 | 4 × 900 | 108 | 4.0 |
| NGC 2962 | 2017 Feb 20 | VPHG1200@540 | 3700–7200 | 6 × 1200 | 172 | 2.5 |
| NGC 3166 | 2006 Apr 28 | VPHG2300G | 4800–5500 | 4 × 1200 | 87 | 2.8 |
| NGC 3166 | 2017 Feb 19 | VPHG1200@540 | 3700–7200 | 4 × 1200 | 87 | 2.5 |
| NGC 3182 | 2014 Mar 31 | VPHG1200@540 | 3700–7200 | 4 × 900 | 153 | 4.0 |
| NGC 3414 | 2009 Mar 30 | VPHG1800R | 6200–7200 | 4 × 900 | 20 | 1.5 |
| NGC 3414 | 2009 Mar 31 | VPHG1800R | 6200–7200 | 5 × 1200 | 150 | 1.3 |
| NGC 3414 | 2010 Apr 10 | VPHG2300G | 4800–5500 | 7 × 1200 | 150 | 3.0 |
| NGC 3619 | 2014 Feb 28 | VPHG1200@540 | 3700–7200 | 3 × 600 | 50 | 3.1 |
| NGC 4026 | 2009 Apr 04 | VPHG1800R | 6200–7200 | 4 × 900 | 178 | 2.8 |
| NGC 4026 | 2012 Apr 18 | VPHG1200@540 | 3700–7200 | 3 × 900 | 176 | 2.5 |
| NGC 7280 | 2009 Oct 12 | VPHG2300G | 4800–5500 | 9 × 1200 | 76 | 1.7 |
| NGC 7280 | 2009 Oct 13 | VPHG2300G | 4800–5500 | 8 × 1200 | 40 | 1.9 |
| NGC 7280 | 2016 Oct 05 | VPHG1800R | 6200–7200 | 4 × 900 | 40 | 1.0 |
| NGC 7280 | 2016 Oct 05 | VPHG1800R | 6200–7200 | 4 × 900 | 76 | 1.4 |
| UGC 9519 | 2012 Apr 20 | VPHG1200@540 | 3700–7200 | 5 × 900 | 75 | 2.0 |
| UGC 12840 | 2014 Nov 14 | VPHG1200@540 | 3700–7200 | 6 × 900 | 15 | 1.1 |

papers (e.g., Sil'chenko et al. 2009). The emission lines, namely, $H\alpha$, $[N II] \lambda 6583$, and $[O III] \lambda 5007$ first of all, were used to derive ionized gas kinematics, by measuring baricenter

positions of the lines; in the central bins, where the stellar continuum is strong, we applied Gaussian analysis to take into account effects of underlying Balmer absorption lines and also

Ti I under [O III] $\lambda 5007$. For the latter purpose, we binned the spectra along the slit to reach S/N higher than 50–70 and then performed a Gaussian analysis of the line complexes [N II] $\lambda\lambda 6548, 6583 + \text{H}\alpha(\text{emission}) + \text{H}\alpha(\text{absorption})$, H $\beta(\text{emission}) + \text{H}\beta(\text{absorption})$, [O III] $\lambda 5007(\text{emission}) + \text{Ti I } \lambda 5007(\text{absorption}) + \text{Ti I } \lambda 5015(\text{absorption})$. With this analysis we are also able to derive the equivalent width of the H α line ($\text{EW}_{\text{H}\alpha}$) and the flux ratios of the strong emission lines: [N II] $\lambda 6583$ to H α , [O III] $\lambda 5007$ to H β , [S II] $\lambda 6717$ to [S II] $\lambda 6731$, and $\Sigma[\text{S II}]$ to H α , which can be used to diagnose the gas excitation mechanisms with the BPT diagrams (Baldwin et al. 1981) and to determine the gas oxygen abundances for the emission-line regions where the gas is excited by young stars. The example of the emission/absorption-line decomposition near the center of NGC 3619 is shown in Figure 2. The sensitivity variations along the wavelength range were corrected by observing spectrophotometric standard stars on the same nights as the galaxies.

As will be noted further, we study the distribution of the above-mentioned emission lines along the slits in more detail for two galaxies—NGC 2551 and NGC 3166. Their spectra demonstrate very extended emission of diffuse ionized gas together with compact bright clumps. For this particular analysis we consider the spatial distribution of the line flux ratios measured by fitting single Gaussians to the observed lines at each position along the slit after subtracting the spectra of stellar population models obtained with the ULYSS software (Koleva et al. 2009), as is shown in Figure 3.

3.2. Observations with the Scanning FPI

Scanning FPI allows us to make a 3D spectroscopic study of the ionized gas kinematics over a large field of view, whereas the narrow interferinge spectral range contains usually only a single emission line selected by a bandpass filter with FWHM of about 15–30 Å. Using the information from the long-slit spectroscopy, we have preliminarily chosen spectral lines in which the most extended ionized gas emission could be expected: H α , [N II] $\lambda 6583$, or [O III] $\lambda 5007$. The targets were observed at the SAO RAS 6 m telescope with SCORPIO-2 in the FPI mode by using the interferometer providing spectral resolution of $\text{FWHM} = 1.7 \text{ \AA}$ ($\sim 78 \text{ km s}^{-1}$) and a full spectral range (interfringe) of $\Delta\lambda = 35 \text{ \AA}$ around the redshifted [N II] or H α line, whereas in the [O III] emission line these parameters were $\text{FWHM} = 2.0 \text{ \AA}$ ($\sim 120 \text{ km s}^{-1}$) and $\Delta\lambda = 20 \text{ \AA}$. During the scanning process, we have consecutively obtained a few tens of interferograms fixing different gaps between the FPI plates covering uniformly the interfringe: 40 frames in the H α or 30 frames in the [O III] spectral ranges. The field of view was 6'.1. The galaxy NGC 3166 was observed with a previous version of the focal reducer SCORPIO in the H α emission line using FPI, providing $\text{FWHM} = 2.5 \text{ \AA}$ ($\sim 112 \text{ km s}^{-1}$) and $\Delta\lambda = 29 \text{ \AA}$; the number of interferograms was 32. The log of the observations, including exposures times and mean seeing values, is presented in Table 3. The data were reduced using the software package described in detail by Moiseev (2002) and Moiseev & Egorov (2008).

Briefly, the used procedures included standard steps for CCD data reduction (bias subtraction, flat-field corrections, sigma clipping of cosmic-ray hits) and some specific steps: removing interference rings related to airglow lines using an azimuthal averaging of brightness in each frame with masked galaxies

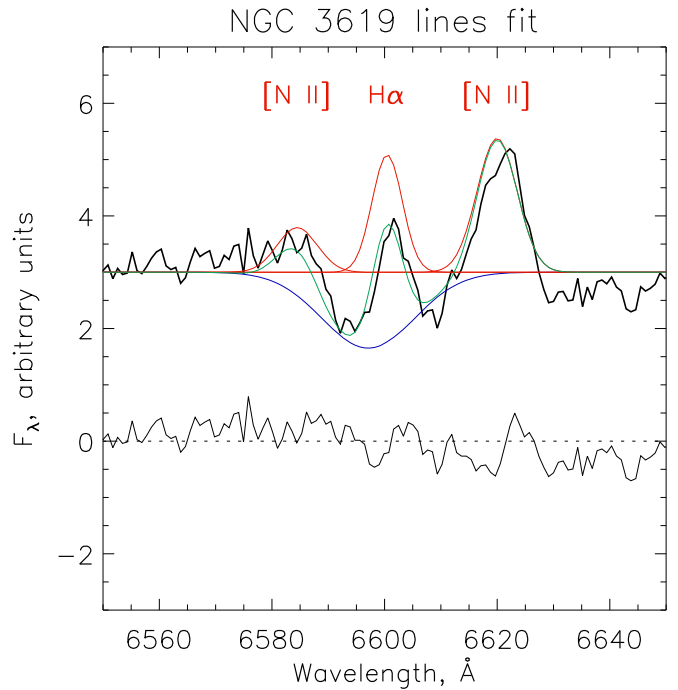


Figure 2. Example of the Gaussian decomposition in the red spectral domain of the H α + [N II] $\lambda\lambda 6548, 6583$ emission lines of the ionized gas (red color) and stellar H α absorption feature (the blue Gaussian) in the observed spectra of NGC 3619 (thick black line). The green line shows the sum of all Gaussians. The thin black line in the bottom shows the residuals after subtraction of the model.

and stars (see Moiseev 2002); correction of atmospheric transparency, as well as seeing variations and astrometric shifts of individual interferograms based on the point-spread function photometry of foreground stars; phase-shift correction (wavelength calibration) based on the scanning of some selected lines in the spectra of an He–Ne–Ar lamp exposed every evening and morning before and after the observational night. After the primary reduction, the observed data are combined into data cubes, where to each spaxel of the field of view a 30-, 32-, or 40-channel spectrum is attributed.

The data cubes were rotated to the “standard” orientation (north at the top). The astrometry grid was created using the Astrometry.net project web interface³ (Lang et al. 2010). The optical continuum and monochromatic images in the emission lines, the line-of-sight velocity fields, and the velocity dispersion maps were created from the one-component Voigt profile fitting of the spectra as described in Moiseev & Egorov (2008). All the velocities presented in the paper are heliocentric.

3.3. Ancillary Data

By wishing to expand our gas velocity fields and to reach a physical interpretation of what we see, for our analysis we involve some additional data on our galaxies that can be retrieved in open data archives. In particular, we use SAURON integral-field unit (IFU) [O III] emission-line data collected in the frame of the ATLAS-3D survey (Cappellari et al. 2011) to refine gas velocity fields in the centers of the galaxies, and we expand our gas velocity fields into the outermost parts of the

³ <http://nova.astrometry.net/>

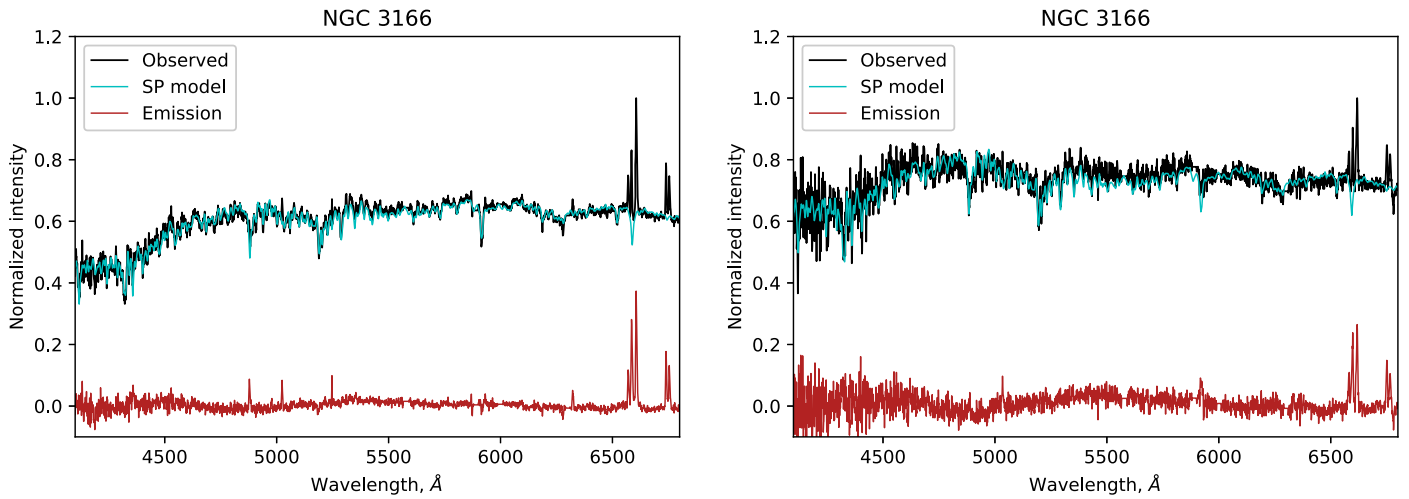


Figure 3. Examples of the pure emission spectrum extraction in low-S/N bins: the emission-line clump in 14'' from the center (left) and an area of diffuse emission in 23'' from the center (right) in the long-slit spectrum of NGC 3166.

Table 3
Log of the Scanning FPI Observations

| Galaxy | Date | Emission Line | Exposure (s) | Seeing (arcsec) |
|-----------|-------------|---------------|----------------------------------|-----------------|
| IC 5285 | 2015 Dec 08 | H α | 40 \times 150 | 2.6 |
| NGC 252 | 2017 Dec 15 | H α | 40 \times 150 | 2.4 |
| NGC 774 | 2014 Nov 13 | H α | 40 \times 240 | 1.0 |
| NGC 2551 | 2015 Dec 08 | H α | 40 \times 180 | 2.1 |
| NGC 2655 | 2015 Dec 07 | [O III] | 30 \times 220 | 2.0 |
| NGC 2697 | 2016 Mar 01 | [O III] | 30 \times 300 | 4.0 |
| NGC 2697 | 2016 Mar 02 | H α | 40 \times 180 | 3.0 |
| NGC 2787 | 2012 Dec 09 | [N II] | 40 \times 180 | 1.7 |
| NGC 2962 | 2016 Feb 29 | H α | 40 \times 180 | 2.2 |
| NGC 3106 | 2015 Dec 09 | H α | 40 \times 120 | 1.4 |
| NGC 3166 | 2007 Feb 14 | H α | 32 \times 160 | 1.3 |
| NGC 3182 | 2014 Feb 28 | H α | 40 \times 160 | 3.0 |
| NGC 3414 | 2016 Feb 15 | [O III] | 30 \times 200 | 2.5 |
| NGC 3619 | 2014 Feb 28 | [O III] | 30 \times 280 | 3.1 |
| NGC 4026 | 2014 Apr 03 | [O III] | 30 \times 180 | 1.8 |
| NGC 4324 | 2016 Feb 29 | H α | 40 \times 180 | 1.8 |
| NGC 7280 | 2014 Nov 18 | [O III] | 30 \times 180 | 1.1 |
| UGC 9519 | 2016 Feb 29 | [N II] | 40 \times 150 | 1.6 |
| UGC 9519 | 2016 May 03 | H α | 40 \times 230 | 1.9 |
| UGC 12840 | 2015 Dec 11 | H α | 34 \times 160 + 6 \times 100 | 1.2 |

galaxies by attaching interferometric HI data (GMRT observations from the archive of <http://wow.astron.nl> presented also in Serra et al. 2012 and Lee-Waddell et al. 2012). The star formation region distributions over the galactic disks are studied with the *GALEX* images (Gil de Paz et al. 2007) obtained in the FUV and near-UV (NUV) bands. The general structure of the galactic disks is considered with the photometric data in the optical bands retrieved from the Sloan Digital Sky Survey (SDSS; <http://www.sdss3.org>) and Pan-STARRS (<https://ps1images.stsci.edu/cgi-bin/ps1cutouts>) archives, as well as with the near-IR (NIR) images of the galaxies in 3.6 and 4.5 μm bands, which have been obtained and made public in the frame of the *Spitzer* telescope galaxy survey S4G (Sheth et al. 2010). Finally, four of our galaxies were observed with the IFU PMAS/PPAK in the frame of the CALIFA survey (Sánchez et al. 2012, 2016; Garcia-Lorenzo et al. 2015), and for these galaxies we have also used the fully reduced data cubes taken from the CALIFA archive, <http://califa.caha.es>.

4. Results

4.1. Kinematics

Figures 4 and 6 present the results of our panoramic and long-slit spectroscopy with the 6 m telescope, respectively. The optical continuum centers are posed to the coordinate zero-points, (0,0) at both axes. The maps are smoothed severely to reach the outermost parts of the gaseous disks, to the typical angular resolution of 2''–3'', so the circumnuclear regions are somewhat poorly resolved. However, in some galaxies a certain turn of the kinematical major axis (defined as the direction of maximum line-of-sight velocity gradient) in the very center is seen: in NGC 3166, NGC 3414, and NGC 7280.

In the central regions of about half of the galaxies their spectral stellar absorption features are rather deep, forcing the faint ionized gas emission lines to sink. In those cases the observed gas kinematics can be strongly affected because the small spectral range of the FPI observations does not allow us to distinguish the contributions of the nebular and stellar

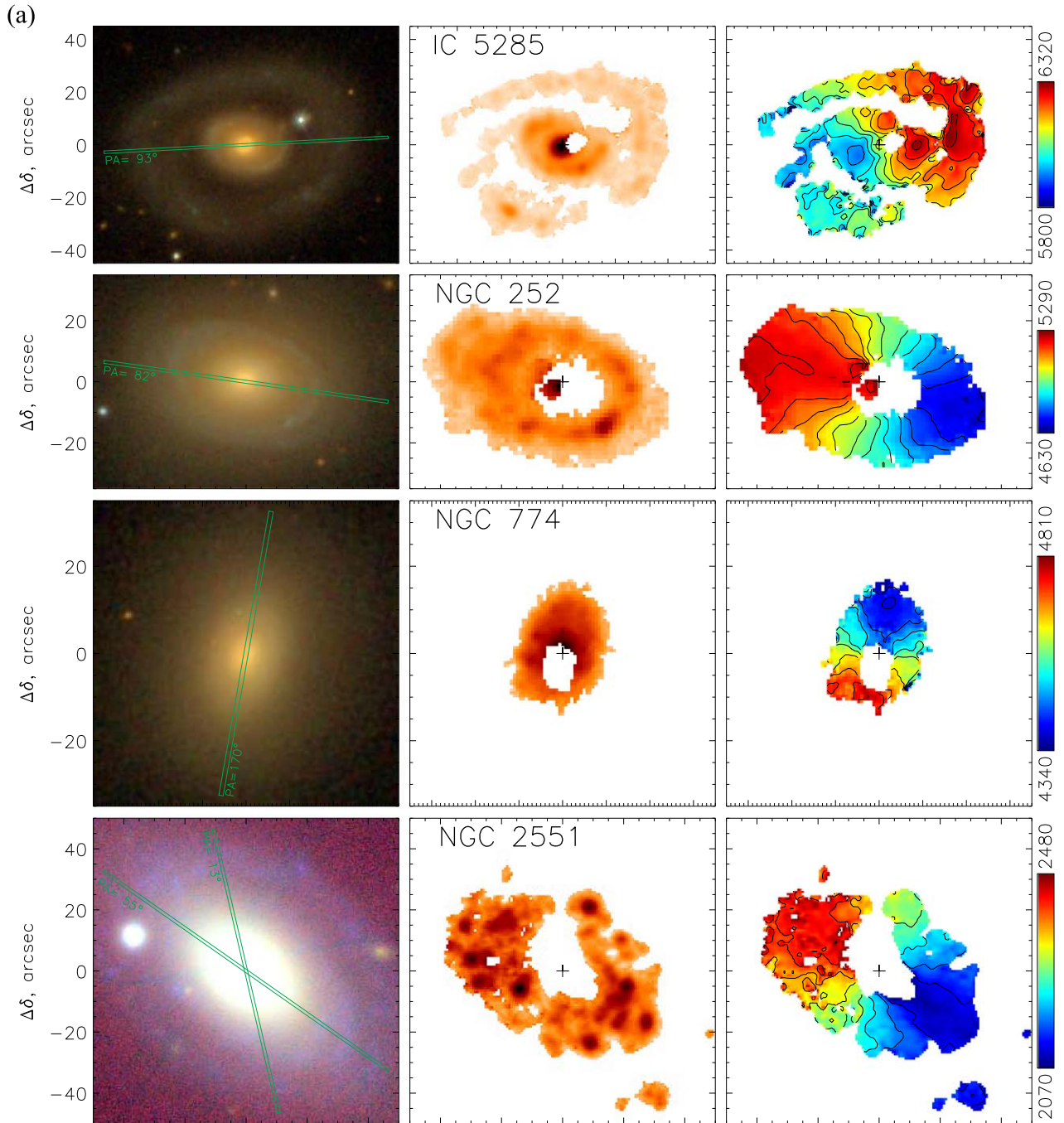


Figure 4. (a)–(d) Optical broadband images of the observed galaxies (left), and the corresponding FPI maps: emission-line images scaled as the square root of the intensity (middle), and ionized gas velocity fields, with the isovelocity contours overplotted through the 50 km s^{-1} step (right). The color bar is in km s^{-1} . The angular offsets are shown with respect to photometric centers of the galaxies. The positions of our long slits with marked PAs are overplotted with green. The combined color images are taken from the SDSS DR14 server; for the targets that were not covered by the SDSS (NGC 2551, NGC 2655, NGC 2697, and NGC 2787) the Pan-STARRS PS1 images are shown, in some cases containing ghosts and color artifacts seen in the original data. (e) For UGC 9519 a combination of the [N II] data for radii less than $20''$ and of the $\text{H}\alpha$ data for the more outer galactic regions is presented.

components into the integrated spectrum. In these cases we could not detect emission lines with the expected velocities in the circumnuclear regions that are blanked in the FPI maps presented in Figure 4. Usually the blanked regions are located asymmetrically relative to the galaxy nucleus (see IC 5285, NGC 774, etc.) because these regions correspond to the maximal contribution of the bulge luminosity against the distant side of the disk. This situation is the inverse of the well-known effect of finding more prominent dust lanes at the

nearest side of a galaxy disk. Concerning the [O III] data, central parts of some emission-line velocity fields are available from the surveys undertaken with the SAURON spectrograph (Bacon et al. 2001; Cappellari et al. 2011). So for NGC 3619 and NGC 4026 we have succeeded in combining the [O III] velocity fields derived from the SAURON data cubes and from our FPI data. Namely, we replaced the central pixels in FPI maps with the SAURON fields if the velocity difference exceeds the limit of about 50 km s^{-1} . In the resulting fields the circumnuclear

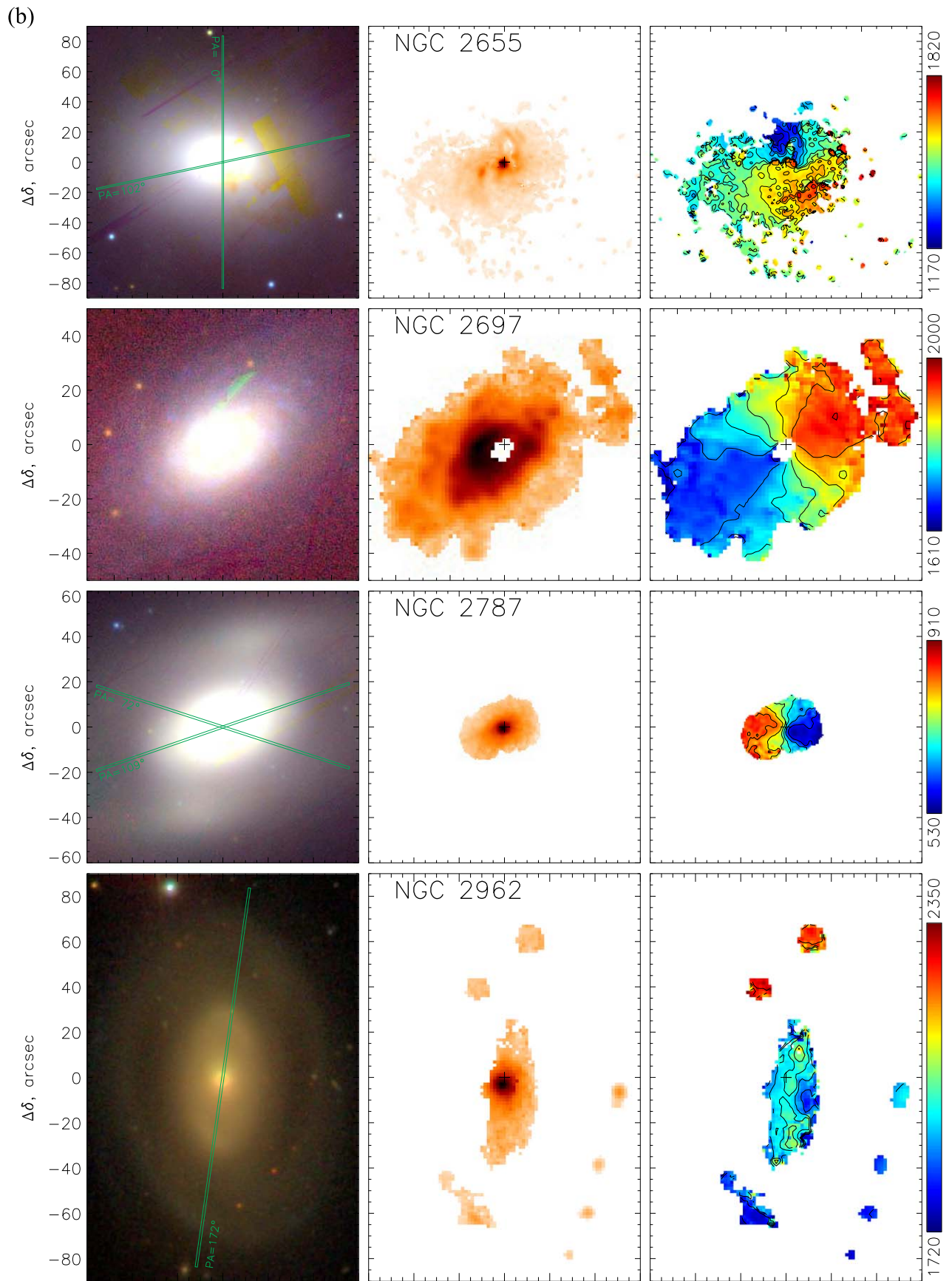


Figure 4. (Continued.)

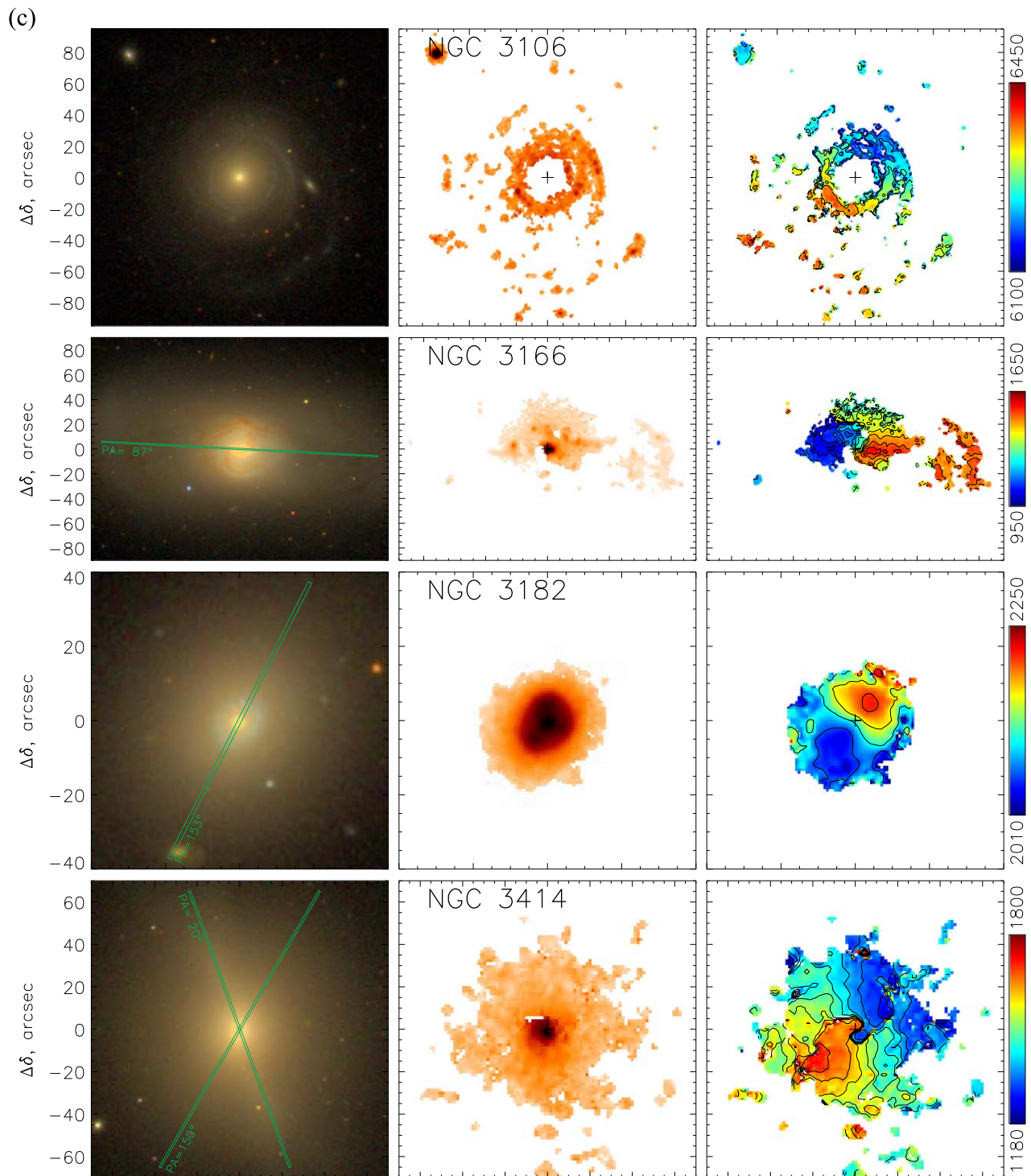


Figure 4. (Continued.)

spaxels (where stellar absorption features are significant) belong to the SAURON data, while the outer regions retain the FPI measurements with a better spectral resolution. Figure 5 illustrates this procedure for NGC 3619. The final “combined” velocity fields were involved further in our analysis described below.

The long-slit cross sections have been mostly obtained with the slit orientation along the photometric major axis, which coincides with the stellar disk line-of-nodes orientation in the case of an intrinsically round stellar disk. The round intrinsic shape of stellar

galactic disks is statistically confirmed more than once, from both photometric (Rix & Zaritsky 1995; Andersen et al. 2001) and kinematical (Franx & de Zeeuw 1992; Cappellari 2016) arguments. However, in some of our galaxies where the kinematical major axes for the gaseous disks derived from the panoramic spectroscopy have been found to deviate strongly from the stellar disk lines of nodes (photometric major axes), we have observed two long-slit spectra with different slit orientations, both being presented in Figure 6; those galaxies are NGC 2655, NGC 2787,

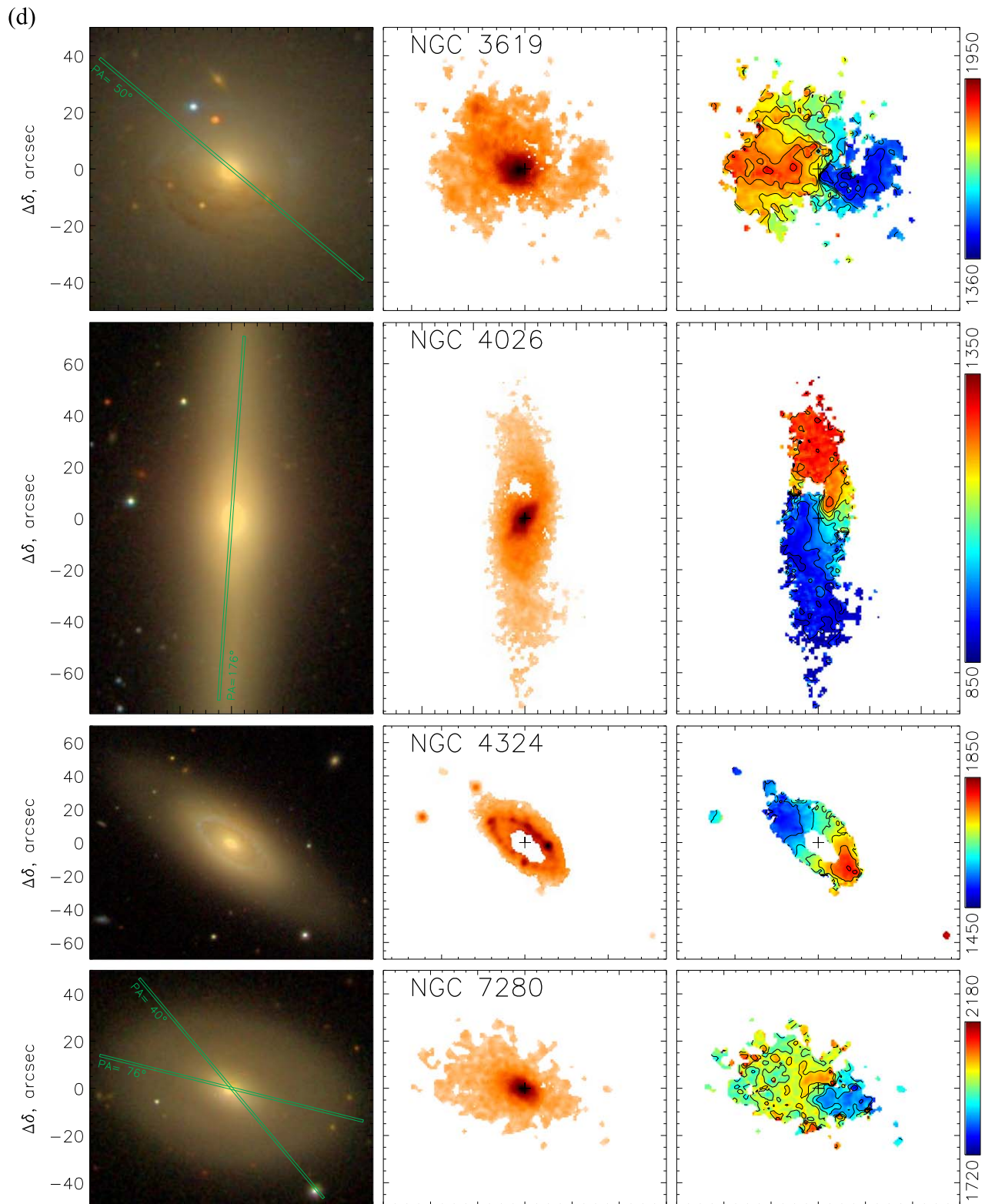


Figure 4. (Continued.)

NGC 3414, and NGC 7280. Below we give some comments on the individual galaxies.

IC 5285. This luminous S0/a galaxy looks like a double-ringed one in continuum, with the outer ring being completely detached from the main disk. Interestingly, being mapped in

the $H\alpha$ emission line, instead of the outer ring, it reveals a pair of gaseous spirals that started from the tips of the inner ring (Figure 4). Perhaps the inner ring borders a triaxial bulge because the major axis of the inner ring is turned with respect to the kinematical major axis; evident noncircular gas motions

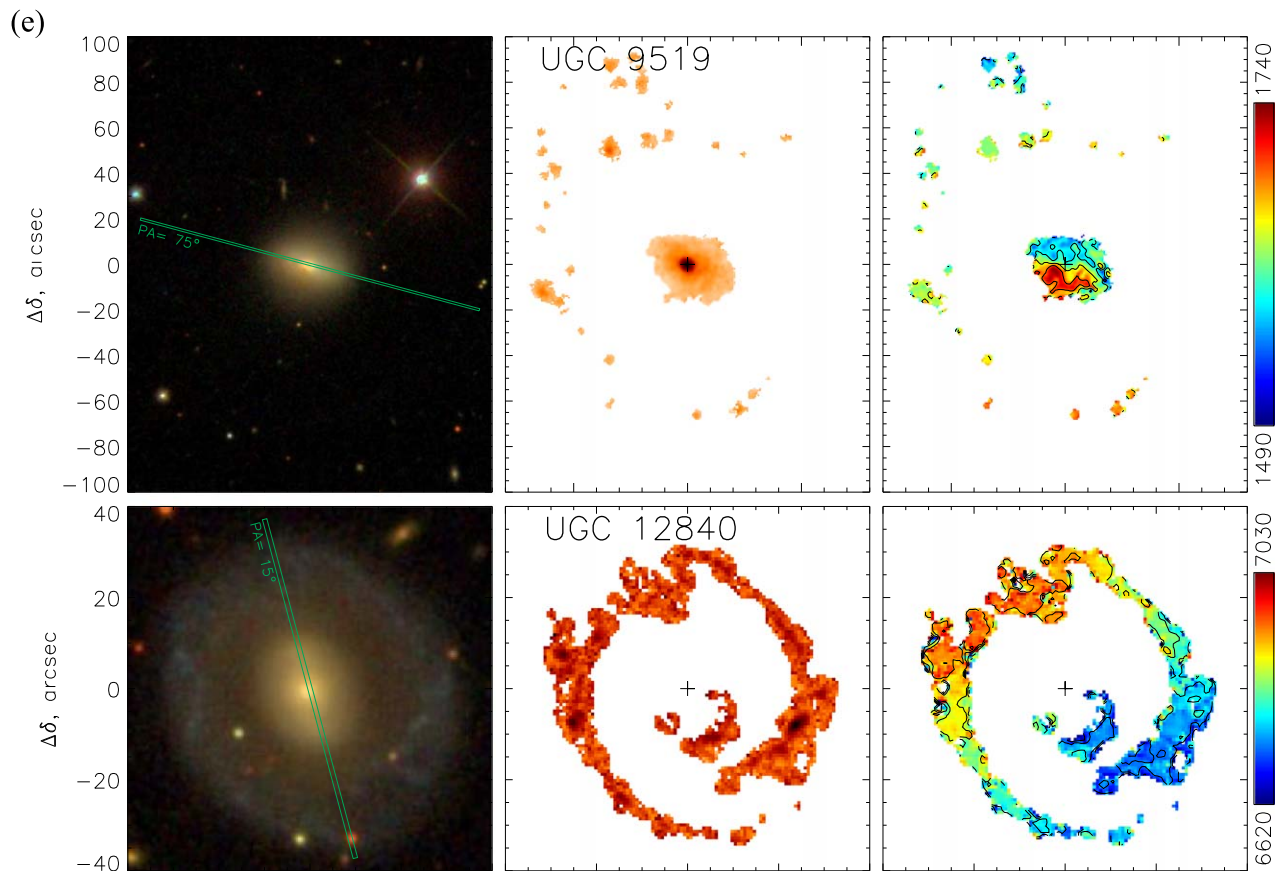


Figure 4. (Continued.)

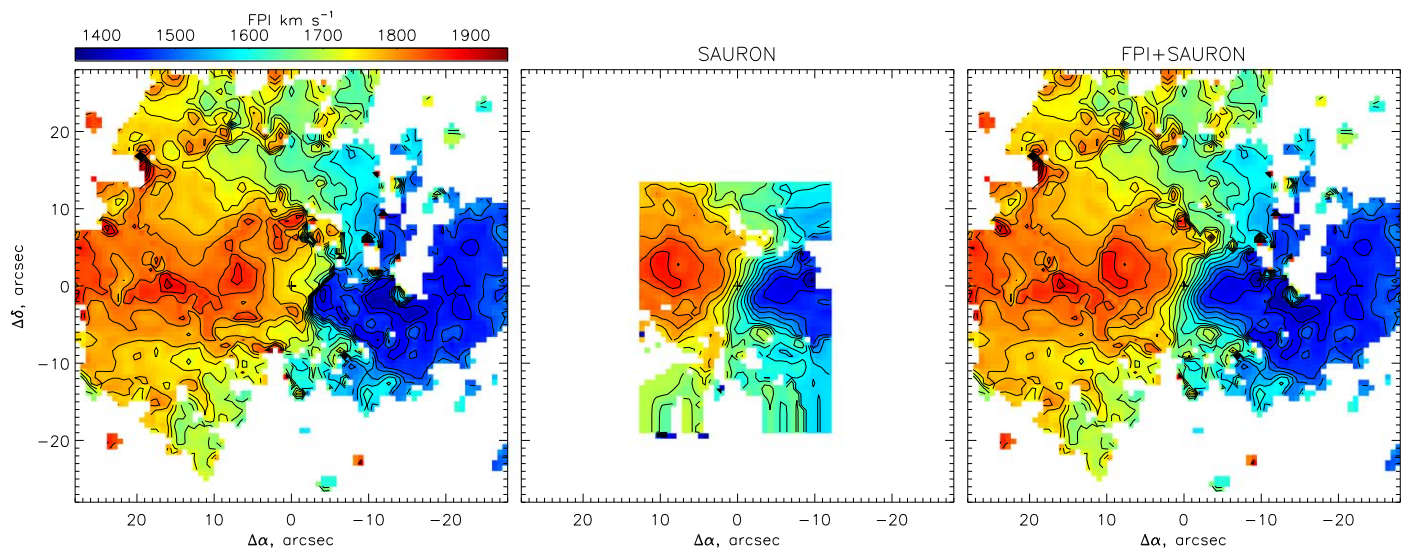


Figure 5. Ionized gas velocity fields in the [O III] emission line for the central region of NGC 3619: the original FPI map (left), the SAURON data in the same spatial and velocity scales (middle), and their combination (right).

are seen in the center of the galaxy. In general, the gaseous disk corotates the stellar component (Figure 6).

NGC 252. The galaxy was reported as a ringed one by Kostyuk (1975). Later we noted a UV ring with a radius about $25''$ and reported gas excitation by young stars in the ring (Ilyina et al. 2014). Now in Figure 4 we present an $H\alpha$ disk extended up to $\sim 40''$ (15 kpc) from the center and rotating with a very high speed, about 350 km s^{-1} . The stars

corotate (Ilyina et al. 2014); the lower visible stellar rotation velocity is perhaps due to asymmetric drift—the stellar disk of NGC 252 may be rather dynamically hot. In the very center, at $R < 7''$, low-excitation emission line [N II] $\lambda 6583$ demonstrates lower rotation velocities than the $H\alpha$ line (Figure 6), implying the possible presence of a triaxial potential, though morphologically the galaxy is classified as unbarred, SA0+.

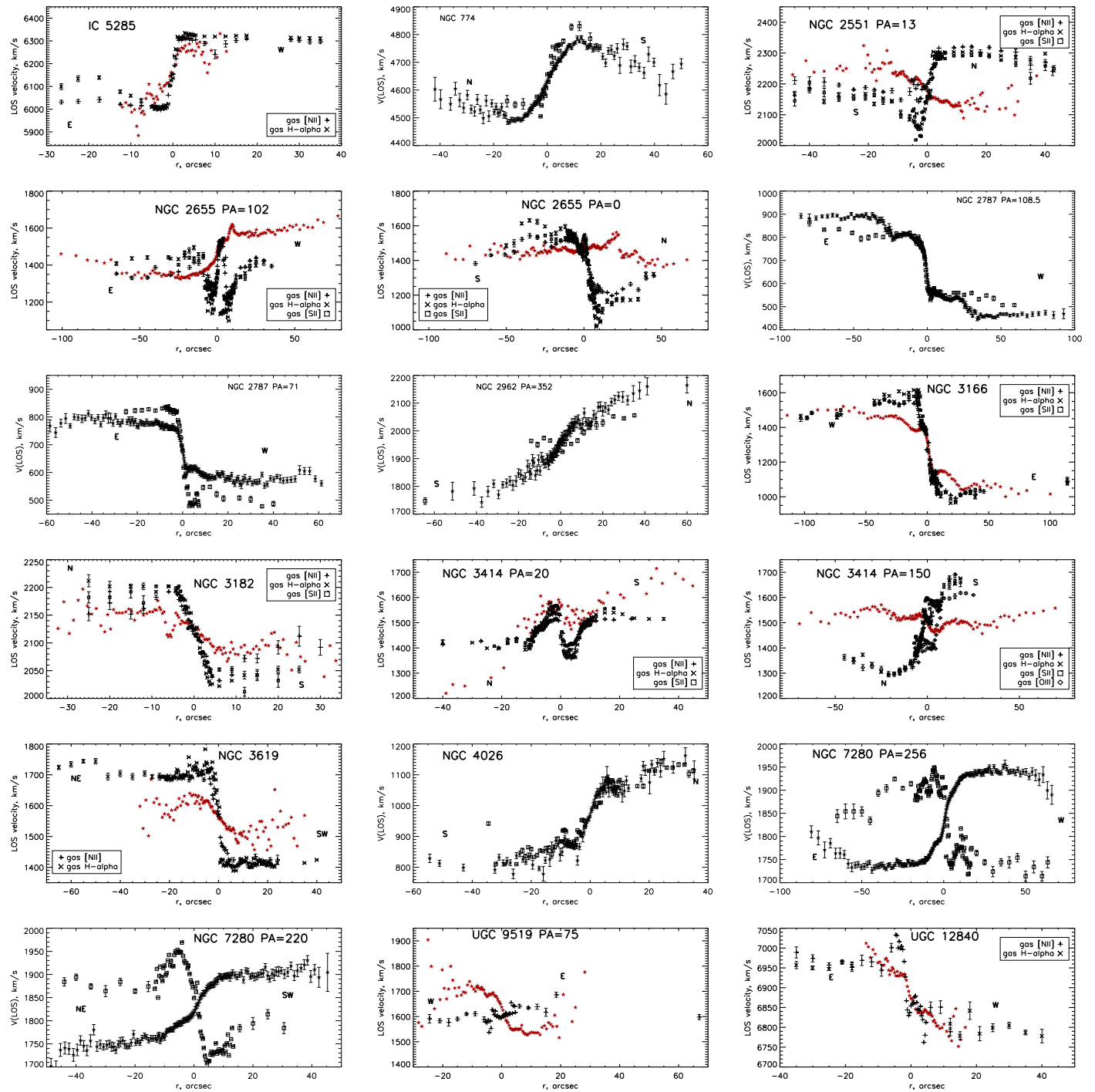


Figure 6. Long-slit line-of-sight velocity profiles obtained with SCORPIO/BTA. Top row: IC 5285 (major axis), NGC 774 (major axis), NGC 2551 (PA = 13°). Second row: NGC 2655 (major axis), NGC 2655 (minor axis), NGC 2787 (major axis). Third row: NGC 2787 (PA = 71°), NGC 2962 (major axis), NGC 3166 (major axis). Fourth row: NGC 3182 (major axis), NGC 3414 (major axis), NGC 3414 (PA = 150°). Fifth row: NGC 3619 (major axis), NGC 4026 (major axis), NGC 7280 (major axis). Bottom row: NGC 7280 (PA = 220°), UGC 9519 (major axis), UGC 12840 (major axis). When only a single emission line is measured (mainly [O III] $\lambda 5007$), it is plotted by squares, and the stellar component rotation is plotted by black stars; when several emission lines are independently measured, they are plotted by various black signs, and the stellar component is indicated by red stars. The abscissa zero corresponds to the brightest-continuum bin along the slit (to the galactic nucleus).

NGC 774. This is another S0 galaxy with a UV ring (Gil de Paz et al. 2007); it must possess even current star formation because recently a core-collapse supernova was detected within the ring (SN 2006ee, 13'' to the SE from the center). The ionized gas is asymmetrically distributed over the central part of the galaxy, within $R < 20''$, or $R < 6$ kpc (Figure 4);

beyond the borders of the gaseous disk the stellar rotation velocity curve falls visibly almost to zero (Figure 6).

NGC 2551. In this galaxy the UV ring is very bright and clumpy in both the FUV and the NUV, and also it is rather wide, from $R \approx 15''$ to $R \approx 30''$ (2–5 kpc; Gil de Paz et al. 2007). The extended ionized gas disk that is coincident radially

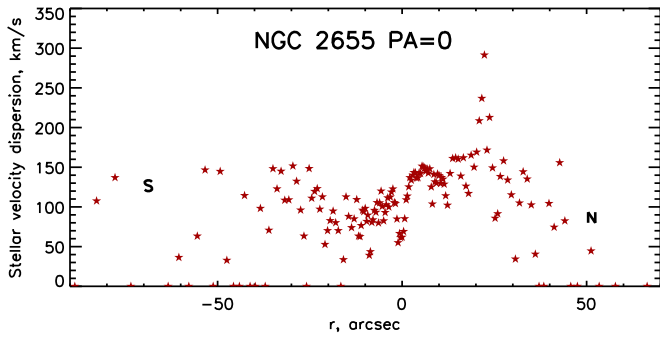


Figure 7. Radial profile of the stellar velocity dispersion along the minor axis of NGC 2655. An increased stellar velocity dispersion can be seen to the north of the nucleus.

with the UV ring (Figure 4) counterrotates as a whole with respect to the stellar disk (Sil'chenko et al. 2009). Earlier we published the long-slit cross section along the disk major axis (Sil'chenko et al. 2009); now we present a cross section under 43° to the line of nodes (Figure 6), confirming the gas counterrotation and also the falling character of the stellar rotation curve.

NGC 2655. This galaxy is an object of long-standing interest to us. Many years ago we started its spectral study with three long-slit cross sections (Sil'chenko & Burenkov 1990); then, we noted that the central part of NGC 2655, $R < 5''$ (0.8 kpc), had quite decoupled gaseous kinematics. Our first interpretation was that it might be an effect of an active nucleus. Later we had made panoramic spectroscopy with the IFU MPFS of the 6 m telescope and had changed our opinion: in the center of NGC 2655 we had detected an inner gaseous disk with *polar* rotation (Sil'chenko & Afanasiev 2004) that had then been supported by a dust lane perpendicular to the isophote major axis (Sil'chenko & Afanasiev 2004). This interpretation was later confirmed by discovery of a strongly warped extended HI disk around NGC 2655 (Sparke et al. 2008). However, now, after inspecting the full LOS velocity field of the ionized gas component (Figure 4) and two orthogonal long-slit cross sections along the major and the minor axes of the isophotes (Figure 6), we are again forced to change our opinion. The general blue–red asymmetry of the gas LOS velocity field is seen in the east–west direction, which is fully consistent with the orientation of the photometric major axis (stellar disk line of nodes). The visible effect of the orthogonal turn of the kinematical major axis near the center is produced by a compact velocity anomaly just to the north and to the west from the nucleus. But when we inspect the long-slit cross sections made under good seeing conditions (Figure 6), we understand that any rotation cannot be the reason of this anomaly: the line-of-sight velocity of the gas drops by some 400 km s^{-1} to the north of the nucleus without any mirrored behavior in the south direction. Interestingly, just in the same place the stellar velocity dispersion rises enormously (Figure 7), betraying the presence of a secondary stellar component with strongly different velocity on our line of sight. Evidently, at $R = 8''$ to the north of the nucleus and along the circumnuclear dust lane to the west of it we see the consequence of minor merging—the remnant of a gas-rich dwarf satellite destroyed by gravitational tides and close in projection to the center of NGC 2655.

NGC 2697. This is a rather low-luminosity S0 galaxy for which no SDSS data were found. We have made our own *gri* photometry, whose results are presented elsewhere (Proshina et al. 2019); in the

same paper we analyze also the long-slit kinematics. Here we note only a well-sampled ionized gas velocity field (Figure 4) demonstrating regular circular gas rotation.

NGC 2787. This is one more galaxy where we searched for an inner polar disk because of the circumnuclear dust lane perpendicular to the isophote major axis (Sil'chenko & Afanasiev 2004). Currently, by exploiting the scanning FPI, we succeeded in tracing the gas rotation in the emission line [N II] $\lambda 6583$ up to $R \approx 20''$, and we saw a turn of the kinematical major axis over this radius range (Figure 4). However, in the emission line [O III] $\lambda 5007$, by comparing the rotation velocity projections for the stars and for the ionized gas exposed with the long slit in two different position angles (Figure 6), we see also decoupled gaseous kinematics at $R > 20''$ quite certainly.

NGC 2962. It is a nearby intermediate-luminosity lenticular galaxy with a detached outer stellar ring at $R \approx 65''\text{--}80''$ (8–10 kpc). The galaxy was included into the survey ATLAS-3D (Cappellari et al. 2011), and so panoramic spectroscopy of its central part, $R < 15''$, with the IFU SAURON had provided us with the orientations of the stellar and the ionized gas rotation planes in its inner part. We found that they are mutually orthogonal (Sil'chenko 2016), so the galaxy possessed the inner polar disk. However, the major axis of the outer ring is aligned with the stellar kinematical major axis, and indeed, our scanning Fabry–Perot data (Figure 4) confirm that the outer gas rotates in the main galactic plane. Our long-slit cross section along the galaxy major axis (Figure 6) reveals both effects—that the rotation axis of the gas within $R = 15''$ is orthogonal to the rotation axis of the stellar component and that at $R \approx 50''\text{--}65''$ the gas rotation comes into consistency with that of the stellar disk. The outer ring of NGC 2962 is well seen in the FUV and NUV bands of the *GALEX* imaging (Marino et al. 2011; see also our Figure 13).

NGC 3106. This galaxy, including its gas velocity field, was studied in the frame of the CALIFA survey (García-Lorenzo et al. 2015). They have found an “outer” star-forming ring in this lenticular galaxy with a radius of some $20''$ (8 kpc; Gomes et al. 2016). However, our data, with a much larger field of view, reveal a series of star-forming rings in NGC 3106 (Figure 4), among which the ring reported by the CALIFA survey is the innermost one. The galaxy is close to face-on; nevertheless, the rotation is visible in Figure 4, and the orientation of the kinematical major axis is measured quite certainly with our data.

NGC 3166. This S0/a galaxy belongs to a tight triplet of disk galaxies embedded into a common HI envelope (Haynes 1981). Many signatures give evidences for the current cold gas accretion onto NGC 3166 from this huge intergalactic gaseous cloud: young age, ~ 2 Gyr, of the nuclear stellar population (Sil'chenko & Afanasiev 2006), large extended molecular gas reservoir within the galaxy disk (Taniguchi et al. 1994), strongly lopsided structure of the large-scale stellar disk (Bournaud et al. 2005), and multiple twisted dust filaments within the central bulge-dominated part of the galaxy (Simoes Lopes et al. 2007). The map in $H\alpha$ emission line (Figure 4) shows also an asymmetric distribution of the ionized gas, with a prominent $H\alpha$ arm at $100''$ (11 kpc) to the west from the nucleus. The gas isovelocitys turn in the very center of the galaxy into a polar orientation. In the outer parts the gas starts to strictly corotate the stars only at $R > 60''$ (Figure 6), where

the large-scale stellar disk begins to dominate in the total surface brightness (Sil'chenko et al. 2012).

NGC 3182. Though the galaxy surely lacks a bar, it demonstrates a circumnuclear blue (star-forming?) ring with a radius of $5''.5$ (0.8 kpc). Beyond the ring, different emission lines show different line-of-sight velocity profiles, the low-ionization [N II] $\lambda 6583$ line being the least rapid, and as a whole the difference between the projected rotation velocities of the gas and stars is unexpectedly large for such a low-mass galaxy. We suspect that this S0 galaxy may possess a thick disk of diffuse ionized gas. Such thick gaseous disks usually lag the fast equatorial plane rotation of galactic stellar disks and demonstrate enhanced low-ionization emission lines [N II] and [S II].

NGC 3414. The real structure of this galaxy remains a complete mystery up to now. It looks like a round homogeneous body (a spheroid? a face-on disk?) with an overlaid thin filament-like structure in the orientation of $PA \approx 20^\circ$. There were various interpretations of such a view: it might be a face-on S0 with a very strong bar (Baggett et al. 1998; Chitre & Jog 2002), but there were also suggestions that it was a face-on S0 with a polar ring projected onto the center (Whitmore et al. 1990). In any case, we were not surprised that the gaseous kinematics in NGC 3414 is completely decoupled from the stellar one (Figure 6). However, in the very center the gas kinematical major axis turns to stay along the thin bar-like structure—we have obtained the same result from our data with the scanning Fabry–Perot in the [O III] $\lambda 5007$ line (Figure 4) and from the archive data obtained earlier for the central part of the galaxy with the IFU SAURON (Sarzi et al. 2006).

NGC 3619. This is another peculiar lenticular galaxy, settling in a rich group and demonstrating a system of outer shells (Schweizer & Seitzer 1988)—possible results of close interaction or even merging. It is rather gas-rich, and the distribution of the neutral hydrogen is unusually compact for S0s (van Driel et al. 1989). In the optical bands, spiral-like dust lanes are projected against the stellar body to the south from the nucleus, implying a circumnuclear gaseous disk settled asymmetrically with respect to the stellar one. A UV-bright inner ring has been detected in the *GALEX* survey (Cortese & Hughes 2009; see also our Figure 13). The distribution of the $H\alpha$ emission is also very asymmetric and extended (Figure 4); however, the ionized gas demonstrates regular rotation with a possible small kinematical major-axis turn in the very center. The rotation velocities of the gas and star components reveal very different projections over the full extension of our measurements (Figure 6), so we may suppose different spatial orientations of the stellar and gaseous disks in NGC 3619.

NGC 4026. This edge-on S0 galaxy belongs to a very rich galaxy group, sometimes classified as a cluster, Ursa Major (Odenwald 1986). The Ursa Major cluster lacks any hot intergalactic medium, so neutral hydrogen streams survive easily within its volume. NGC 4026 has been studied in the frame of the ATLAS-3D survey (Cappellari et al. 2011), and a substantial amount of neutral hydrogen has been detected not only within its disk but also as a narrow external filament connecting just to the galaxy center (Serra et al. 2012). Thus, we expected decoupled gaseous rotation in this galaxy. Indeed, in the very center the [O III] $\lambda 5007$ line demonstrates a rapidly rotating gaseous disk strongly inclined to the stellar disk—this is seen in our Figure 4, as well as in the IFU SAURON emission-line data (Sil'chenko 2016). However, beyond the

central region, the ionized gas is strictly confined to the stellar disk, and its rotation follows the stellar component one exactly (Figure 6).

NGC 4324. This lenticular galaxy inhabits outskirts of the Virgo Cluster, and it is very gas-rich (see the Table 1). It is also a part of the ATLAS-3D survey (Cappellari et al. 2011) and demonstrates a blue star-forming ring with a radius of some 2 kpc, which also contains all the molecular gas detected so far (Alatalo et al. 2013). However, Duprie & Schneider (1996) detected HI up to two optical radii in this galaxy, which gave hope that ionized gas also may be extended beyond the inner star-forming ring. Indeed, in Figure 4 we see clumpy outer star-forming regions up to $R \approx 70''\text{--}90''$ (7.5 kpc) from the center; most of them take part in the general regular rotation of the gaseous disk. However, a few—for example, that to the northeast from the galaxy—do not participate in the rotation of NGC 4324 and may be gas-rich satellites.

NGC 7280. This is one more lenticular galaxy that has attracted our attention for many years. Once, we had found an inner polar gaseous ring in the center of NGC 7280 (Afanasiev & Sil'chenko 2000). Later, in the frame of the ATLAS-3D survey, it was confirmed that the neutral hydrogen distribution in this galaxy is indeed aligned with the polar axis (Serra et al. 2012). This galaxy was treated as a gas-rich S0 from the beginning (Chamaraux et al. 1987), and star formation was carefully searched for in its disk (Pogge & Eskridge 1993). But there was no current star formation found in the disk of NGC 7280. Instead, we have discovered *counterrotation* of the ionized gas with respect to the stars beyond the central region, at $R > 10''$ (Sil'chenko 2005). Now, with a full map of the ionized gas velocities (Figure 4), we confirm the central compact polar disk; the outer gas is distributed asymmetrically and counterrotates with respect to the stars (Figure 6).

UGC 9519. This is a dwarf lenticular galaxy elongated in $PA = 75^\circ$. However, in the frame of the ATLAS-3D survey an outer HI ring was found by Serra et al. (2012), well beyond the optical borders of the galaxy, which is elongated in the north–south direction. The long-slit cross section along the isophote major axis (Figure 6) has confirmed the decoupled kinematics of the gas and its probable external origin. To obtain a full picture, we have observed UGC 9519 with the scanning FPI in two emission lines, $H\alpha$ and [N II] $\lambda 6583$. Our anticipation was justified: the inner part of the galaxy, $R < 15''$, is well mapped just in the emission line [N II] $\lambda 6583$, while in the outer part we resolve the outer star-forming ring only in the $H\alpha$ emission line; Figure 4 represents a combination of the [N II] data for radii less than $20''$ and of the $H\alpha$ data for the more outer galactic regions. The inner gas rotates in the nearly polar plane with respect to the stellar disk, and the outer ionized gas, being related surely to the neutral hydrogen detected by Serra et al. (2012), is quite decoupled from the main body of the galaxy.

UGC 12840. This galaxy is a giant, isolated (Karachentseva 1973), gas-rich lenticular one. Just in *this* galaxy Pogge & Eskridge (1993) had found extended star formation in the outer ring. We also detect a giant ring, with a radius of some 12.5 kpc, emitting in the $H\alpha$ emission line (Figure 4). Though the galaxy looks almost round, $b/a > 0.8$, the projection of the rotation velocity is large, $\sim 100 \text{ km s}^{-1}$, and the ionized gas corotates strictly the stellar component. Some noncircular gas motions are possible in the very center of the galaxy.

4.2. Tilted Ring Analysis to Understand the Character of the Gas Motions

The benefit of 2D velocity fields representing spatially resolved projection of rotation velocities at various distances from the galactic centers onto our line of sight is that we can check the circular character of the ionized gas rotation and derive the spatial orientation of the rotation plane if the rotation is circular, lacking strong radial motions, expansions, or inflows. Indeed, in the case of circular rotation the maximum rotation velocity projection onto the line of sight is observed at the line of nodes; in its turn, the intrinsically round stellar disk looks like an ellipse with the isophote major axis coincident with the line of nodes. So when the gas is confined to the plane of the galactic disk and while its rotation is circular, we should see the steepest gradient of the observed line-of-sight velocity (“kinematical major axis”) along the isophote major axis. If the gas rotation is noncircular, which must be the case within a nonaxisymmetrical potential, the kinematical and photometric major axes would turn *in the opposite sense* with respect to the line of nodes (Vauterin & Dejonghe 1997). Finally, if we see that the gas kinematical major axis does not coincide with the stellar disk line of nodes, but this deviation is not accompanied by the symmetric deviation of the photometric major axis *within the same radial range*, it means that the rotation plane of the ionized gas stands in the space differently from the plane of the stellar disk.

By assuming ionized gas *planar circular* rotation within some running radial range, we can derive two angles of its spatial orientation, in general varying along the radius: an inclination of the disk plane to our line of sight and a position angle of its line of nodes tracing gas plane intersection with the sky plane. We have made it by applying to the gas line-of-sight velocity fields a tilted ring analysis (Begeman 1989) adopted for the ionized gas FPI data. For this purpose we have used the IDL software DETKA, as described by Moiseev et al. (2004) and Moiseev (2014). The method is based on splitting the observed velocity field into elliptical rings (1”–5” wide) oriented according to adopted inclination i_0 and line-of-sight position angle of the disk PA_0 . In all observed galaxies the center of symmetry of a velocity field lies no further than 1”–2” from the photometric nucleus (the center of the inner isophotes); therefore, the galaxy nuclei were fixed as the ring centers. The χ^2 minimization was used to fit the observed velocity distribution within every ring by model of quasi-circular rotation with the following parameters: kinematical major axis PA_{kin} , inclination i , rotation velocity V_{rot} , and systemic velocity V_{sys} . As a null approximation for PA_0 and i_0 we adopted the orientation parameters according to the photometric data (HyperLEDA and isophotal analysis results). During the next steps, we fixed often the V_{sys} derived at the first step. When the patchy character of a velocity field prevented a stable minimization over three parameters, we chose to fix first the inclination i and then PA_{kin} ; V_{rot} remained always free. Sometimes we applied an iterative procedure, fixing i and PA_{kin} by turns. The i and PA_{kin} were also always fixed in the outer regions, where the elliptical rings contain only a few points in the velocity fields. We also masked some local regions notable for their peculiar kinematics, deviating by more than 30–50 km s⁻¹ from the obtained model; this threshold was individually tuned.

Unfortunately, in most cases the direct tilted ring fitting described above gives unstable solutions just for $i(r)$ owing to

noise and holes in the ionized gas velocity fields. The uncomfortable problem consists of unphysical chaotic changes of the V_{rot} induced by strong derived variations of i with radius. The well-known degeneracy between these two quantities was discussed by numerous authors (Begeman 1989; Kamphuis et al. 2015). To avoid this problem, we performed the following evaluation of the $i(r)$ behavior based on the first-step tilted ring analysis results. Namely, at every r we extracted from the velocity field an elliptical ring oriented in agreement with i_0 and $PA_{\text{kin}}(r)$ obtained as described above. Then we fitted the velocities in the ring using only two free parameters: i and V_{rot} , whereas the PA_{kin} and V_{sys} were already obtained at this radius and fixed. The next step was to repeat the procedure by fixing the obtained $i(r)$ and by leaving PA_{kin} free to refine it. Finally, we were able to obtain stable fitting results with a reasonable shape of the rotation curve for the considered galaxies, in their central regions as a minimum. The results of this study, including the analysis of the HI velocity fields available in the references, are presented in Sections 5.2–5.4.

The comparison of the kinematical major axis orientations running along the radius with the stellar disk lines of nodes is given in Figure 8. In these plots presenting the tilted ring analysis results we have also overlaid the results of isophote analysis—the radial variations of the photometric major-axis position angles. The lines of nodes are fixed from the outermost isophote major-axis orientation (sometimes taken outside the plotted radial range). In some cases we have also gotten the orientations of the kinematical major axes for the *stellar* components; they are obtained with the same DETKA software by applying it to the data from the ATLAS-3D survey (Cappellari et al. 2011) or from the CALIFA survey (Sánchez et al. 2012, 2016). In these cases we can check independently the circular shape of the stellar disk and the axisymmetry of the gravitational potential.

A quick look at Figure 8 reveals a great variety of behavior of the gas kinematical major axis in the gas-rich lenticular galaxies. Sometimes the ionized gas lies in the galactic planes and exhibits regular circular rotation (NGC 252, NGC 2551, NGC 4324), though the gaseous disk plane may be warped *together* with the stellar plane (NGC 252), or the gas may counterrotate the stellar rotation (NGC 2551; Sil'chenko et al. 2009). Sometimes the gas lies within the decoupled plane homogeneously inclined to the stellar disk (NGC 2655, NGC 3619). Sometimes the central gas is in the polar plane, but at larger radii it comes to the main galactic plane—and starts to corotate the stellar disk (NGC 2962, NGC 4026) or counterrotate it (NGC 7280, Figure 6) or to form a completely detached outer star-forming ring (UGC 9519). Sometimes the central region of a galaxy (its bulge?) looks triaxial, with a twisted isophote major axis, but the ionized gas just within the same radial range remains to be confined to the plane of the stellar disk and demonstrates regular circular rotation (IC 5285, UGC 12840, NGC 3106). And the last is perhaps the most interesting class of objects: those with the ionized gas confined to the galactic planes and demonstrating laminar circular rotation, but *only within a limited radial range*—NGC 774, NGC 2697, NGC 3166, NGC 3182. This last case will be discussed in more detail in Section 5.

4.3. Gas Excitation and Metallicities

The source of ionized gas excitation can be determined by analyzing the flux ratios of low-ionization and high-ionization

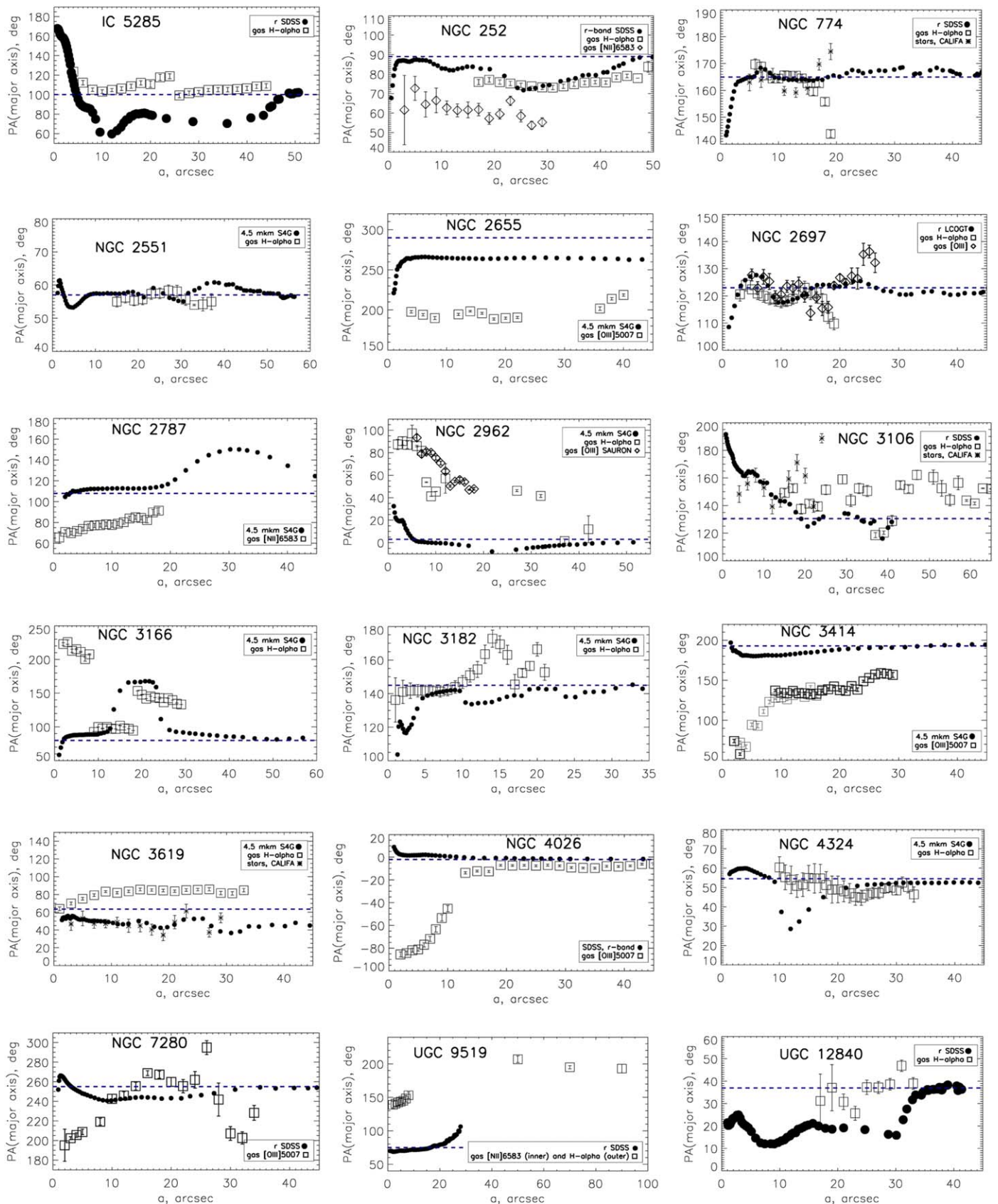


Figure 8. Comparison of the photometric and kinematical major-axis orientations; sometimes the orientation of the kinematical stellar disk line of nodes is also shown following the analysis of the SAURON or CALIFA panoramic spectral data. The horizontal dashed lines indicate orientations of the stellar disk lines of nodes determined from the position angles of the outermost isophotes.

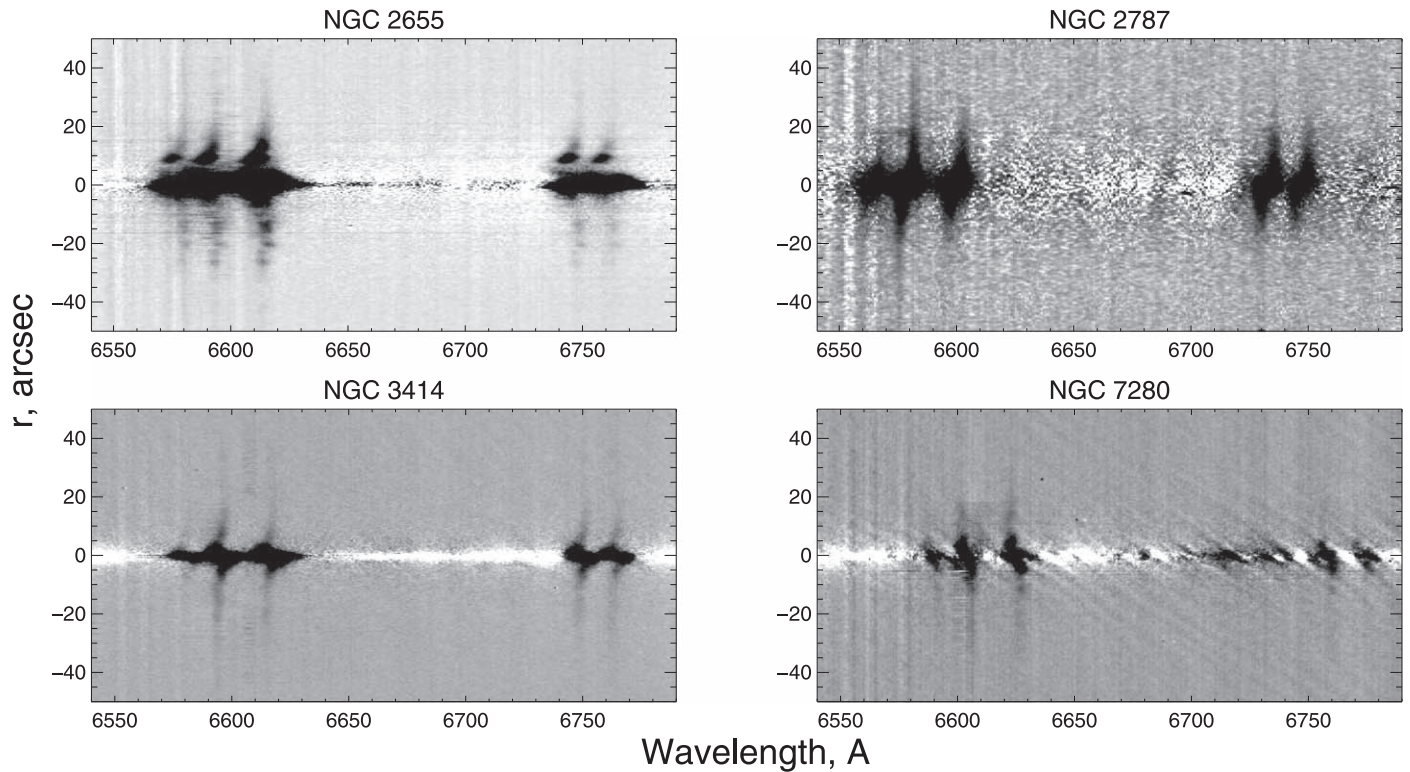


Figure 9. Example of long-slit spectra obtained along the major axes of the four galaxies demonstrating almost homogeneous enhanced emission in [N II] and [S II] lines. Stellar continuum and absorption lines were modeled with ULYSS and subtracted.

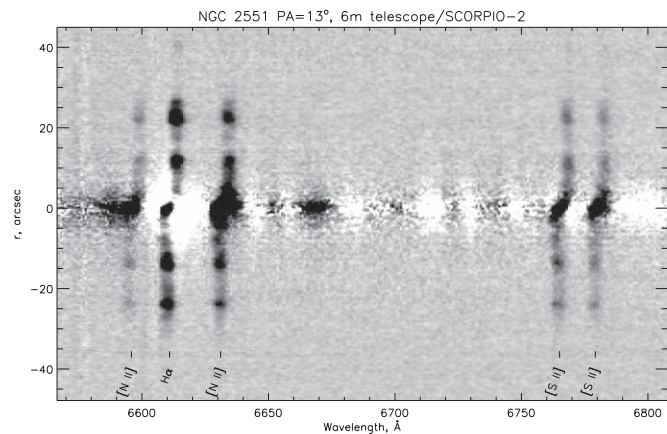


Figure 10. Example of the clumpy emission lines in the long-slit spectrum of NGC 2551—the S0 galaxy with a broad star-forming ring.

emission lines to Balmer emission lines—at so-called BPT (Baldwin–Phillips–Terlevich) diagrams (Baldwin et al. 1981; Veilleux & Osterbrock 1987). At the least, star-forming regions demonstrate quite recognizable emission-line spectra, and the models allow us to determine the chemical composition—mainly oxygen abundances—by using the flux ratios of strong emission lines just for the case of the gas excited by young stars. We have checked the gas excitation in our S0 galaxies by studying the emission lines in the long-slit spectra obtained with SCORPIO/BTA; for NGC 774 and NGC 3106 we have used the public spectral data cubes from the CALIFA survey (Sánchez et al. 2016), and for NGC 2697 and NGC 4324 additional spectral data obtained earlier at the 11 m SALT of the SAAO with the

long-slit spectrograph RSS (Proshina et al. 2019) have been incorporated into our present analysis. The gaseous disks with strongly decoupled rotation—those in NGC 2655, NGC 2787, NGC 3414, and NGC 7280—have all demonstrated shock-like excitation: in their spectra the emission line [N II] λ 6583 is comparable to or even stronger than the H α everywhere along the slit (see 2D spectra obtained along major axes of the mentioned galaxies in Figure 9). A similar pattern of emission-line ratios is typical for diffuse ionized gas (DIG), which gives commonly a possibility to explain diffuse gas excitation in early-type galaxies by old, strongly evolved stars (Binette et al. 1994). The other galaxies demonstrate inhomogeneous clumpy emission-line distributions along the slit (see the example of such behavior in Figure 10), and we have measured the emission-line flux ratios for the individual clumps. We show the BPT diagrams for these measurements in Figure 11. The emission from the regions lying under the theoretical “maximum starburst line” from Kewley et al. (2001) can be in principle explained through photoionization by young stars, but the composite mechanism of excitation might be responsible for the emission from the clumps lying between this line and the empirical Kauffmann et al. (2003) separating sequence. As follows from Figure 11, half of the clumps in NGC 3166 and some regions in NGC 2551 clearly demonstrate dominating mechanisms of gas excitation different from photoionization by young stars (e.g., by shocks or by old, post-AGB stars). The NGC 774 ring lies at the border between the H II-region-like excitation and DIG-like or shock-like excitation. All other resolved clumps lie well below the “maximum starburst line,” around the Kauffmann et al. (2003) H II-fitting sequence, and their emission can be explained through pure photoionization by young massive stars. Hence, we can

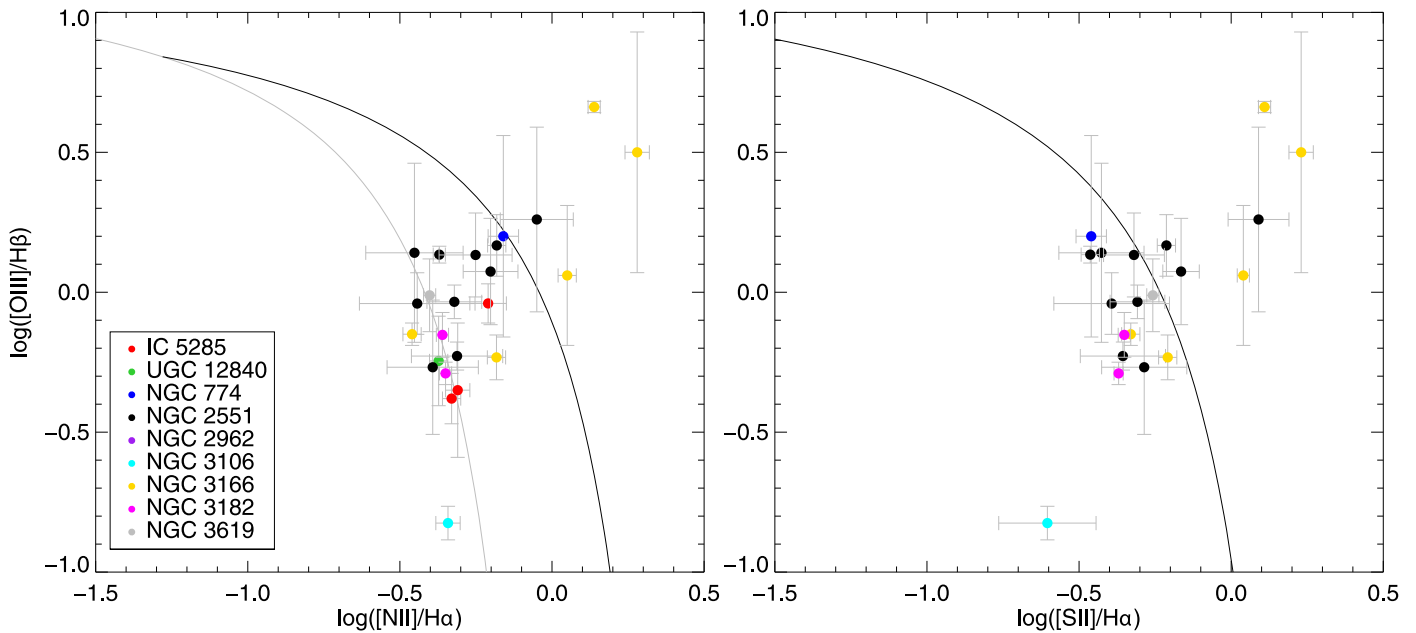


Figure 11. BPT diagrams for some radial zones in nine S0 galaxies with extended emission. The curves separating H II regions from all other types of gas excitation are from Kewley et al. (2001) (black solid curve) and from Kauffmann et al. (2003) (gray solid curve).

determine oxygen abundances of the gas in these clumps by exploring strong-line methods.

In general, accurate oxygen abundances in H II regions can be “directly” derived from measurements of electron temperature-sensitive line ratios, such as $[\text{O III}] \lambda\lambda 4959, 5007 / [\text{O III}] \lambda 4363$. This is often referred to as the T_e -method. However, in most cases it is impossible to measure faint emission lines like $[\text{O III}] \lambda 4363$ in distant galaxies. To avoid this problem, many empirical and model-based calibrations relying on strong emission lines only were developed. Despite that, the well-known problem of discrepancy (up to 0.6 dex) of various metallicity calibrations is still not resolved (see, e.g., Kewley & Ellison 2008). Here we have used several empirical methods to derive oxygen abundances $12 + \log(\text{O}/\text{H})$ and have compared their results. Because of the limited spectral range of our data, we selected only those methods that do not demand the $[\text{O II}] \lambda\lambda 3727, 3729$ line to be observed: S-method (Pilyugin & Grebel 2016), O3N2, N2 (both from Marino et al. 2013), and D16 (Dopita et al. 2016). The first three of these methods were calibrated using local H II regions with well-known oxygen abundances determined through the T_e -method. The fourth method, D16, is a photoionization-model-based one.

Every method used by us has its advantages and disadvantages in comparison with others. Thus, only the $[\text{N II}]/\text{H}\alpha$ ratio is needed for the N2 method, but it is applicable only for $8.0 < 12 + \log(\text{O}/\text{H}) < 8.65$, gives very large scatter (0.16 dex at 1σ level) of the yielding values, and hence provides only a rough estimate of the gas metallicity. Another popular method—O3N2—uses neighboring emission-line ratios, $[\text{O III}]/\text{H}\beta$ and $[\text{N II}]/\text{H}\alpha$, and hence almost does not suffer from uncertainties with reddening correction. This method is applicable within $8.17 < 12 + \log(\text{O}/\text{H}) < 8.77$ and shows large dispersion (on average 0.18 dex, but significantly lower for $12 + \log(\text{O}/\text{H}) > 8.4$). Recent studies have shown that the contamination by a large fraction of DIG affects the results obtained with the O3N2 method in only a small extent (Kumari et al. 2019; Poetrodjojo et al. 2019). The S-method is well calibrated in the range of $7.1 < 12 + \log(\text{O}/\text{H}) < 8.75$ and on testing the sample yields results

that agree with estimations made by using the T_e -method, with a standard deviation of ~ 0.05 dex. In its original form this method suffers from reddening uncertainties (which are rather high in our data) because all involved emission-line fluxes ($[\text{O III}]$, $[\text{S II}]$, $[\text{N II}]$) should be normalized to the flux of the $\text{H}\beta$ line. Finally, the D16 method demands only flux ratios of the lines within the red part of a spectrum— $[\text{N II}]/[\text{S II}]$ and $[\text{N II}]/\text{H}\alpha$. This method was developed for application to high- z galaxies, and its main advantage is that it does not depend on the ionization parameter or interstellar medium pressure, and hence it might be used safely also for regions having enhanced $[\text{N II}]/\text{H}\alpha$ ratios (e.g., lying in the composite excitation zone at the BPT diagrams). However, note that it is still calibrated through the photoionization models that do not include excitation by shocks. This method yields systematically higher oxygen abundances (in comparison with the T_e -method) because of the higher solar abundance used as a zero-point in calibration ($12 + \log(\text{O}/\text{H}) = 8.77$ instead of 8.69). Unfortunately, authors of the original work do not provide an estimate of the typical uncertainty for the D16 calibration.

Taking into account the problems with the metallicity calibrations used in this work, we have applied some corrections to the results, making them more comparable with each other:

1. All the values of $12 + \log(\text{O}/\text{H})$ obtained with the D16 method were reduced by 0.08 dex to take into account the different solar oxygen abundance values assumed.
2. As an input for the S-method, we have used the $[\text{S II}]/\text{H}\alpha$ and $[\text{N II}]/\text{H}\alpha$ line flux ratios and a proposed theoretical Balmer decrement $\text{H}\alpha/\text{H}\beta = 2.86$ (Osterbrock & Ferland 2006). This correction allowed us to reduce significantly the final uncertainty of the oxygen abundance by getting rid of uncertainties with the reddening estimates.
3. All the values beyond the area of applicability of the method used were considered wrong ones.

The results of the excitation analysis and oxygen abundance estimates are based on the observed flux ratios presented in Table 4 and are summarized in Table 5, where different columns correspond to name of the galaxy; projected distance

Table 4
Emission-line Ratios in the Rings of S0 Galaxies

| Galaxy Name ^a | Radius (arcsec) | EW(H α) (Å) | log([N II] λ 6583/H α) | log([O III] λ 5007/H β) | log([S II] λ 6717 +6731/H α) | [S II] λ 6717/ λ 6731 | H α /H β |
|--------------------------|--------------------|---------------------|--|--|--|---------------------------------------|-----------------------|
| I5285 | -12 | 5.6 | -0.21 \pm 0.06 | -0.04 \pm 0.07 | | | |
| | +16 | 24.3 | -0.33 \pm 0.03 | -0.38 \pm 0.09 | | | |
| | +31 | 31.4 | -0.31 \pm 0.04 | -0.35 \pm 0.24 | | | |
| U12840 | -20 | 20.9 | -0.37 \pm 0.03 | -0.21 \pm 0.16 | | | 5.8 \pm 0.9 |
| N774 ^b | 9 | 2.0 \pm 0.3 | -0.16 \pm 0.05 | +0.20 \pm 0.36 | -0.46 \pm 0.05 | 0.76 \pm 0.07 | >7 |
| N2551 | -29 | 7.2 | -0.45 \pm 0.16 | +0.17 \pm 0.32 | -0.41 \pm 0.14 | 1.5:: | 5.1 \pm 2.7 |
| | -24 | 13.8 | -0.31 \pm 0.15 | -0.20 \pm 0.05 | -0.34 \pm 0.14 | >1.5 | 5.0 \pm 1.2 |
| | -20 | 7.0 | -0.44 \pm 0.19 | +0.00 \pm 0.11 | -0.37 \pm 0.19 | >1.5 | 6.4 \pm 3.2 |
| | -17 | 4.75 | -0.39 \pm 0.15 | -0.24 \pm 0.24 | -0.27 \pm 0.14 | 1.38 \pm 0.16 | 5.0 \pm 3.1 |
| | -14 | 5.8 | -0.32 \pm 0.09 | -0.02 \pm 0.06 | -0.30 \pm 0.09 | 1.52 \pm 0.07 | 3.8 \pm 0.2 |
| | +12 | 3.9 | -0.18 \pm 0.03 | +0.19 \pm 0.11 | -0.20 \pm 0.03 | 1.29 \pm 0.10 | 4.5 \pm 0.7 |
| | +15.5 | 1.0 | -0.05 \pm 0.12 | +0.26 \pm 0.33 | +0.09 \pm 0.10 | 1.06 \pm 0.19 | 2.15 \pm 1.1 |
| | +19 | 2.8 | -0.20 \pm 0.09 | +0.10 \pm 0.19 | -0.15 \pm 0.06 | 1.22 \pm 0.11 | 4.8 \pm 1.9 |
| | +23 | 14.0 | -0.37 \pm 0.02 | +0.14 \pm 0.03 | -0.46 \pm 0.03 | 1.37 \pm 0.08 | 3.2 \pm 0.3 |
| | +27 | 6.9 | -0.25 \pm 0.12 | +0.15 \pm 0.15 | -0.31 \pm 0.10 | 1.42 \pm 0.12 | 4.0 \pm 1.9 |
| | N3106 ^b | 21W | 22.5 | -0.34 \pm 0.04 | -0.80 \pm 0.06 | -0.59 \pm 0.16 | 1.12 \pm 0.15 |
| N3106 ^b | 21E | 43.5 | -0.34 \pm 0.04 | -0.80 \pm 0.06 | -0.59 \pm 0.16 | 1.12 \pm 0.15 | 4.7 \pm 0.2 |
| N3166 | -98 | ∞ | -0.46 \pm 0.03 | -0.15 \pm 0.04 | -0.33 \pm 0.03 | 1.33 \pm 0.15 | |
| | -72 | 118 | +0.14 \pm 0.02 | +0.68 \pm 0.02 | +0.12 \pm 0.02 | 1.42 \pm 0.07 | 4.1 \pm 0.2 |
| | -27 | 4.2 | +0.05 \pm 0.03 | +0.06 \pm 0.25 | +0.04 \pm 0.02 | 1.14 \pm 0.03 | >7 |
| | +14 | 1.7 | +0.28 \pm 0.04 | +0.50 \pm 0.43 | +0.23 \pm 0.04 | 1.14 \pm 0.06 | >7 |
| | +28 | 13.3 | -0.18 \pm 0.03 | -0.20 \pm 0.08 | -0.19 \pm 0.03 | 1.36 \pm 0.09 | 5.5 \pm 0.4 |
| N3182 | -5.5 | 13.7 | -0.35 \pm 0.02 | -0.29 \pm 0.04 | -0.37 \pm 0.015 | 1.32 \pm 0.05 | 2.1 \pm 0.4 |
| | +5.5 | 12.2 | -0.36 \pm 0.02 | -0.15 \pm 0.08 | -0.35 \pm 0.02 | 1.31 \pm 0.07 | 3.0 \pm 1.0 |
| N3619 ^c | 20 | 8.9 \pm 0.5 | -0.40 \pm 0.02 | +0.02 \pm 0.13 | -0.24 \pm 0.02 | 1.37 \pm 0.05 | 5.3 \pm 0.9 |

Notes.

^a Galaxy ID—N = NGC, U = UGC, I = IC.

^b CALIFA data.

^c CALIFA+SCORPIO data.

of the current clump from the galactic center, in orientation according to Figure 6; the color excess $E(B - V)$ derived from the observed Balmer decrement; electron density n_e derived from the [S II] λ 6717/ λ 6731 flux ratios (Osterbrock & Ferland 2006) assuming $T_e = 10,000$ K; BPT_{N2} and BPT_{S2} parameters—the offsets from the “maximum starburst line” at the corresponding BPT diagram; and the oxygen abundance $12 + \log(\text{O}/\text{H})$ derived using four methods described above. The listed uncertainties of the oxygen abundances derived do not include systematic uncertainties of the methods, which should be added quadratically.

As follows from Table 5, for most of the star-forming clumps all the methods yield values of oxygen abundance consistent with each other within their uncertainties. The strong discrepancies are observed for the clumps in NGC 2551 and NGC 3166, demonstrating a non-H II-like mechanism of excitation (BPT_{S2} > 0 and/or BPT_{N2} > 0)—the estimated values of oxygen abundance are not reliable for them. High discrepancy is also observed for the only clump in NGC 774 located in the transition zone of the BPT diagram with the N2 abscissa axis and having the highest electron density among all studied objects.

5. Discussion

5.1. Star-forming Rings in the Disk Planes of S0 Galaxies

We have checked the galaxies of our sample in the MAST Archive to see whether they are detected in the UV with GALEX. Indeed, most of them (12 of 18) are detected in the

FUV band of the GALEX survey (Gil de Paz et al. 2007), and their UV morphology usually looks ring-like. The UV images of the sample galaxies are shown in Figure 13. High-contrast ring-like UV structures are clearly visible even in galaxies without rings of very recent star formation traced by the optical emission lines (e.g., NGC 774, NGC 3619, etc.).⁴ The UV rings in NGC 3619 and NGC 4324 were reported earlier by Cortese & Hughes (2009), the UV ring in NGC 2962 was reported by Marino et al. (2011), and the UV ring in NGC 252 was earlier studied by us through long-slit spectroscopy with SCORPIO of the Russian 6 m telescope in the optical spectral range (Ilyina et al. 2014). The results of the gas excitation analysis within the area of UV-bright rings have shown that the UV-bright rings in S0 galaxies have mostly emission-line spectra typical for the gas excited by young massive stars betraying current star formation. However, there are two interesting cases where we have resolved a change of the gas excitation mechanism along the radius. In NGC 2551 at the *inner northern* edge of the star-forming ring series, $R = 12''$ – $19''$, the excitation mechanism is composite—the excitations by young stars and by shock waves are both involved, and the electron density is increased just at this radius. In NGC 3166 the distribution of the UV surface brightness is not symmetric with respect to the center; it is

⁴ The central “holes” in the FPI maps of some galaxies (IC 5285, NGC 774, etc.) are caused by the strong H α absorption line in the galactic spectra produced by the underlying stellar population, not by star-forming rings. We could not take this effect into account because the spectral range of the FPI data is too small.

Table 5
Excitation and Metallicity Diagnostic Results

| Name | R (arcsec) | $E(B - V)$ | n_e (cm $^{-3}$) | BPT $_{N2}$ | BPT $_{S2}$ | $12 + \log(O/H)$ | | | |
|-----------|--------------|-----------------|---------------------|-------------|-------------|------------------|-----------------|-----------------|-----------------|
| | | | | | | S | O3N2 | N2 | D16 |
| IC 5285 | -12.0 | ... | ... | -0.17 | ... | ... | 8.50 ± 0.02 | 8.65 ± 0.04 | ... |
| IC 5285 | 16.0 | ... | ... | -0.40 | ... | ... | 8.54 ± 0.02 | 8.59 ± 0.03 | ... |
| IC 5285 | 31.0 | ... | ... | -0.37 | ... | ... | 8.54 ± 0.05 | 8.60 ± 0.03 | ... |
| UGC 12840 | -20.0 | 0.61 ± 0.13 | ... | -0.40 | ... | ... | 8.51 ± 0.04 | 8.57 ± 0.03 | ... |
| NGC 774 | 9.0 | ... | 1320 | -0.01 | -0.11 | 8.75 ± 0.04 | 8.46 ± 0.08 | ... | 8.97 ± 0.10 |
| NGC 2551 | -29.0 | 0.50 ± 0.46 | ... | -0.28 | -0.11 | 8.52 ± 0.13 | 8.41 ± 0.08 | 8.53 ± 0.08 | 8.55 ± 0.25 |
| NGC 2551 | -24.0 | 0.48 ± 0.21 | ... | -0.33 | -0.20 | 8.59 ± 0.13 | 8.52 ± 0.04 | 8.60 ± 0.07 | 8.65 ± 0.24 |
| NGC 2551 | -20.0 | 0.70 ± 0.43 | ... | -0.38 | -0.16 | 8.51 ± 0.16 | 8.45 ± 0.05 | 8.54 ± 0.09 | 8.52 ± 0.31 |
| NGC 2551 | -17.0 | 0.48 ± 0.54 | 50 | -0.42 | -0.14 | 8.50 ± 0.14 | 8.51 ± 0.06 | 8.56 ± 0.07 | 8.48 ± 0.24 |
| NGC 2551 | -14.0 | 0.25 ± 0.05 | ... | -0.27 | -0.08 | 8.58 ± 0.08 | 8.47 ± 0.03 | 8.59 ± 0.05 | 8.59 ± 0.15 |
| NGC 2551 | 12.0 | 0.39 ± 0.13 | 120 | -0.05 | 0.09 | 8.69 ± 0.03 | 8.46 ± 0.03 | ... | 8.67 ± 0.05 |
| NGC 2551 | 15.5 | ... | 390 | 0.11 | 0.40 | 8.76 ± 0.13 | 8.47 ± 0.08 | ... | 8.54 ± 0.18 |
| NGC 2551 | 19.0 | 0.45 ± 0.34 | 190 | -0.11 | 0.09 | 8.65 ± 0.08 | 8.47 ± 0.05 | 8.65 ± 0.05 | 8.60 ± 0.13 |
| NGC 2551 | 23.0 | 0.10 ± 0.08 | 50 | -0.22 | -0.14 | 8.59 ± 0.02 | 8.42 ± 0.02 | 8.57 ± 0.03 | 8.69 ± 0.04 |
| NGC 2551 | 27.0 | 0.29 ± 0.41 | 20 | -0.12 | -0.02 | 8.65 ± 0.10 | 8.45 ± 0.04 | 8.63 ± 0.06 | 8.69 ± 0.19 |
| NGC 2962 | -63.0 | ... | 940 | ... | ... | ... | ... | 8.47 ± 0.08 | 8.21 ± 0.19 |
| NGC 3106 | 21.0 | 0.43 ± 0.04 | 300 | -0.69 | -0.58 | 8.64 ± 0.06 | 8.64 ± 0.02 | 8.59 ± 0.03 | 8.87 ± 0.19 |
| NGC 3166 | -98.0 | ... | 80 | -0.44 | -0.14 | 8.47 ± 0.03 | 8.47 ± 0.02 | 8.53 ± 0.03 | 8.44 ± 0.05 |
| NGC 3166 | -72.0 | 0.31 ± 0.04 | 20 | 0.50 | 0.62 | ... | 8.42 ± 0.01 | ... | 8.76 ± 0.03 |
| NGC 3166 | -27.0 | ... | 280 | 0.11 | 0.28 | ... | 8.53 ± 0.06 | ... | 8.71 ± 0.04 |
| NGC 3166 | 14.0 | ... | 280 | 0.52 | 0.64 | ... | 8.49 ± 0.09 | ... | 8.82 ± 0.07 |
| NGC 3166 | 28.0 | 0.56 ± 0.06 | 60 | -0.21 | -0.06 | 8.66 ± 0.03 | 8.54 ± 0.02 | ... | 8.67 ± 0.05 |
| NGC 3182 | -5.5 | ... | 90 | -0.39 | -0.23 | 8.57 ± 0.02 | 8.52 ± 0.02 | 8.58 ± 0.03 | 8.62 ± 0.03 |
| NGC 3182 | 5.5 | 0.04 ± 0.29 | 100 | -0.35 | -0.17 | 8.56 ± 0.02 | 8.49 ± 0.02 | 8.58 ± 0.03 | 8.59 ± 0.03 |
| NGC 3619 | 20.0 | 0.53 ± 0.15 | 50 | -0.33 | -0.03 | 8.50 ± 0.02 | 8.45 ± 0.03 | 8.56 ± 0.03 | 8.44 ± 0.03 |

lopsided, with the most UV radiation emitted to the west from the nucleus. And the only radial zone in NGC 3166 that demonstrates the H II-region-like emission-line spectrum is the western distant (tidal?) arm. All other emission-line rings in NGC 3166 have shock-like or composite gas excitation. Despite the presence of a large-scale bar in NGC 3166, we would conclude, therefore, that its ring-like emission-line structures have probably a tidal or impact origin due to interaction with the neighboring members of the group, NGC 3169 and NGC 3165, and cold gas accretion from the common H I group envelope (see Section 5.2).

We must discuss here that not only in the case of shocks but also in the case of DIG domination the enhanced [N II], [S II], and [O III] lines might be observed. Among the sources considered to be responsible for DIG excitation are the radiation of old hot pAGB stars (Sokolowski & Bland-Hawthorn 1991; Binette et al. 1994), the leakage of hard photons from the star-forming regions (Hoopes & Walterbos 2003), and the shock waves (see discussion in Zhang et al. 2017). As was argued by, e.g., Flores-Fajardo et al. (2011), low-mass evolved stars might be relevant sources of the gas ionization in S0 galaxies. To consider whether the possible contribution of the DIG affects our conclusion about the presence of shocks in some regions of NGC 2551 and NGC 3166, we made the following analysis. We identified the regions crossed by our slits that might be related to the DIG. Various criteria of this exist in the literature: Zhang et al. (2017) proposed to use the H α emission-line surface luminosity as an indicator; after conversion to the observed

flux per pixel, $F(H\alpha) < 7.4 \times 10^{-17}$ erg s $^{-1}$ cm $^{-2}$ should be considered as DIG excited by old stars. At the same time, according to Lacerda et al. (2018), $EW(H\alpha) < 3 \text{ \AA}$ is expected to be a more precise indicator. In Figure 12 we demonstrate the obtained radial profiles of the logarithm of the H α line flux, $EW(H\alpha)$, and emission-line flux ratios for each galaxy. In the second panel from the top we marked those regions showing $EW(H\alpha) > 3 \text{ \AA}$ (and hence surely not related to old stars) by squares, while the regions that might be considered as the DIG are shown by circles. Note that both mentioned criteria can disagree in particular regions. Since we expect a uniform distribution of the old stars in a galaxy, we may also expect a similar distribution of their contribution to the ionization. After excluding the areas with $EW(H\alpha) > 3$ and the central part of the galaxies ($R < 5''$ for NGC 2551, $R < 10''$ for NGC 3166; the ionization conditions in these regions might significantly differ from the rest of the galaxy, and this is beyond the scope of our analysis), we have performed a second-order robust polynomial fitting of the flux logarithm distribution along the slit. The result is shown in the second panel of Figure 12 by a solid line. The same fitting was performed for every emission line analyzed; the obtained smooth models were subtracted from the observed fluxes. After that, we compared the emission-line flux ratios in the BPT diagrams (bottom panel of Figure 12) before (red color) and after (blue color) correction for the DIG contribution. As follows from these plots, the performed correction changes the position in the BPT diagrams of the points classified by us as DIG but almost does not influence the

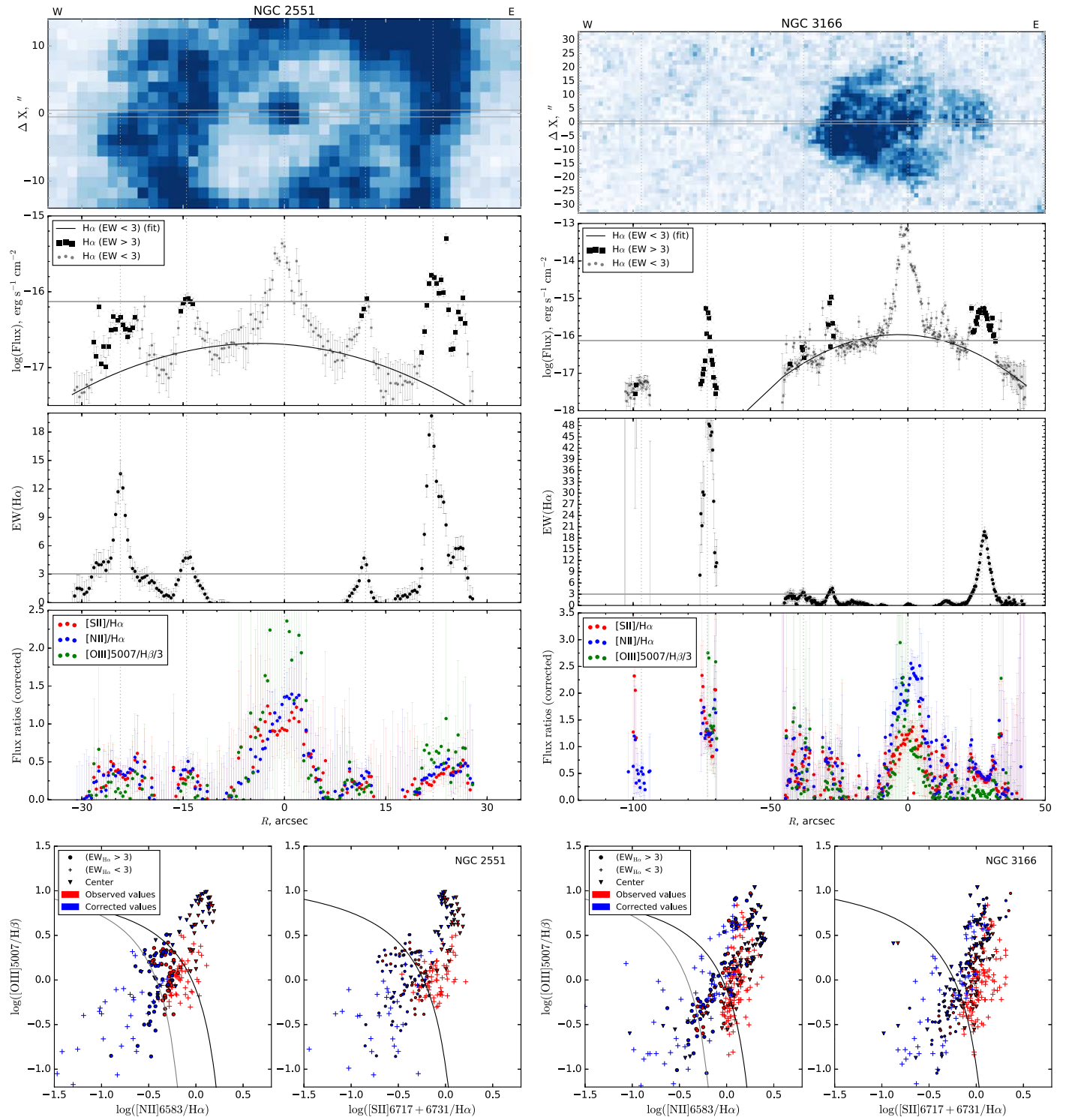


Figure 12. Analysis of the ionization state along the slit for the galaxies NGC 2551 (left) and NGC 3166 (right). From top to bottom: position of the slit overlaid on the FUV image (*GALEX*) of the galaxies; distribution of the $H\alpha$ line flux (horizontal line denotes a level of $F(H\alpha) = 7.4 \times 10^{-17} \text{ erg s}^{-1} \text{ cm}^{-2}$ used to identify the DIG regions by Zhang et al. 2017; curved line shows the polynomial fit of the DIG flux distribution); $EW(H\alpha)$ (horizontal line corresponds to the value of $EW(H\alpha) = 3 \text{ \AA}$ used to identify the DIG regions by Lacerda et al. 2018); emission-line flux ratios corrected for the DIG contribution; BPT diagrams constructed for individual pixels along the slit. In the BPT diagram red shows observed flux ratios while blue shows that corrected for the DIG contribution. Different symbols denote the galactic center and regions with $EW(H\alpha) > 3 \text{ \AA}$ or $EW(H\alpha) < 3 \text{ \AA}$. The curves separating H II regions and all other types of gas excitation are from Kewley et al. (2001) (black solid curve) and from Kauffmann et al. (2003) (gray solid curve).

flux ratios in the regions with $EW(H\alpha) > 3 \text{ \AA}$ that were considered earlier as shocks or star-forming rings. Hence, we may conclude that the presence of the DIG does not change our conclusions concerning the gas excitation mechanisms in the emission-line clumps. Note, however, that we cannot exclude

the contribution of the filtered hardened radiation from H II regions in star-forming rings to the enhancement of [N II], [S II], and [O III] lines. The DIG component ionized by the filtered radiation may be more structured than one ionized by low-mass evolved stars considered above. Hence, one may still

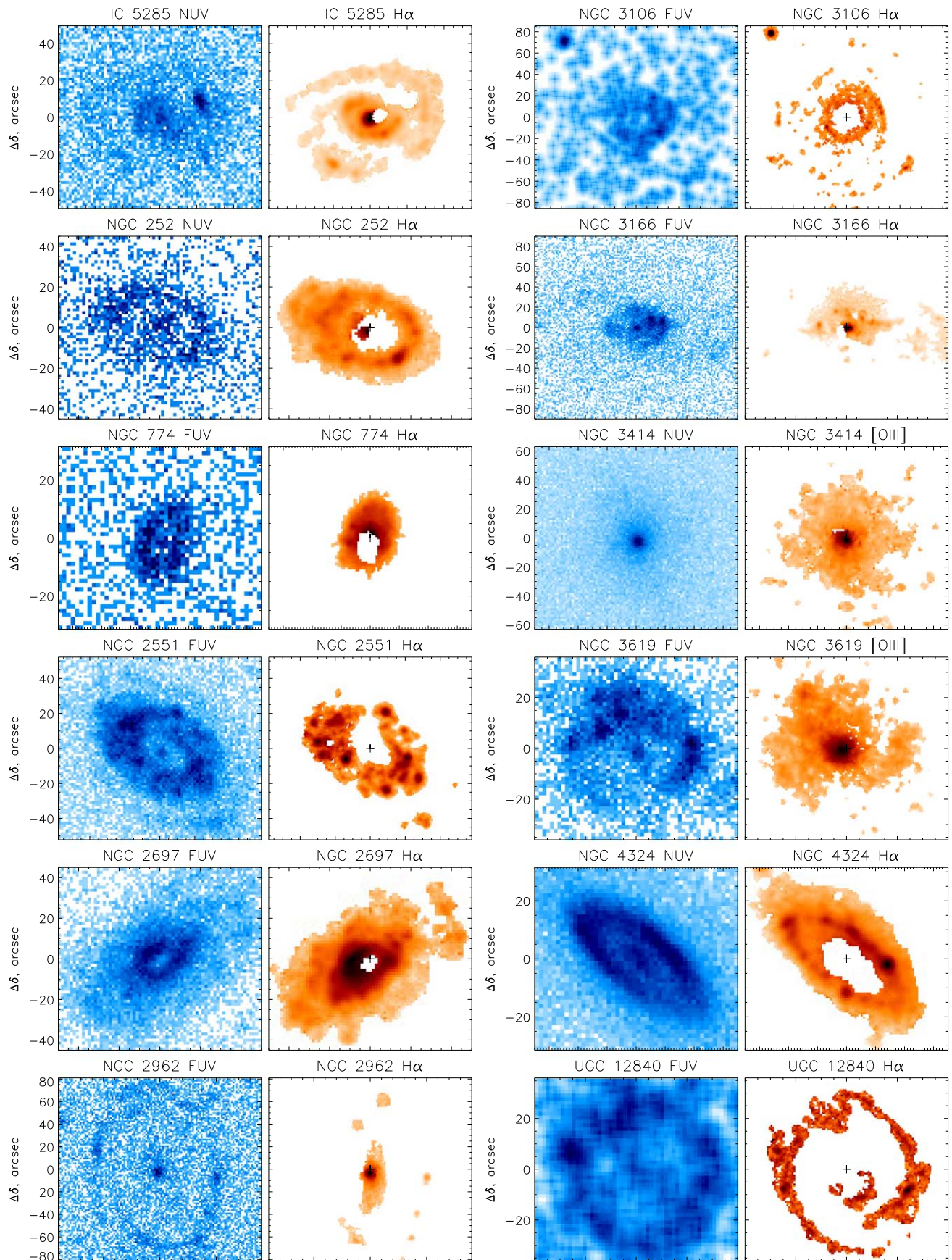


Figure 13. *GALEX* images of the sample galaxies observed in the FUV and sometimes the NUV bands (if the deep FUV data were not available). The emission-line images from SCORPIO/FPI of the 6 m telescope are also shown for comparison. The scale is a square root of intensity. The star-forming rings are detected in most cases.

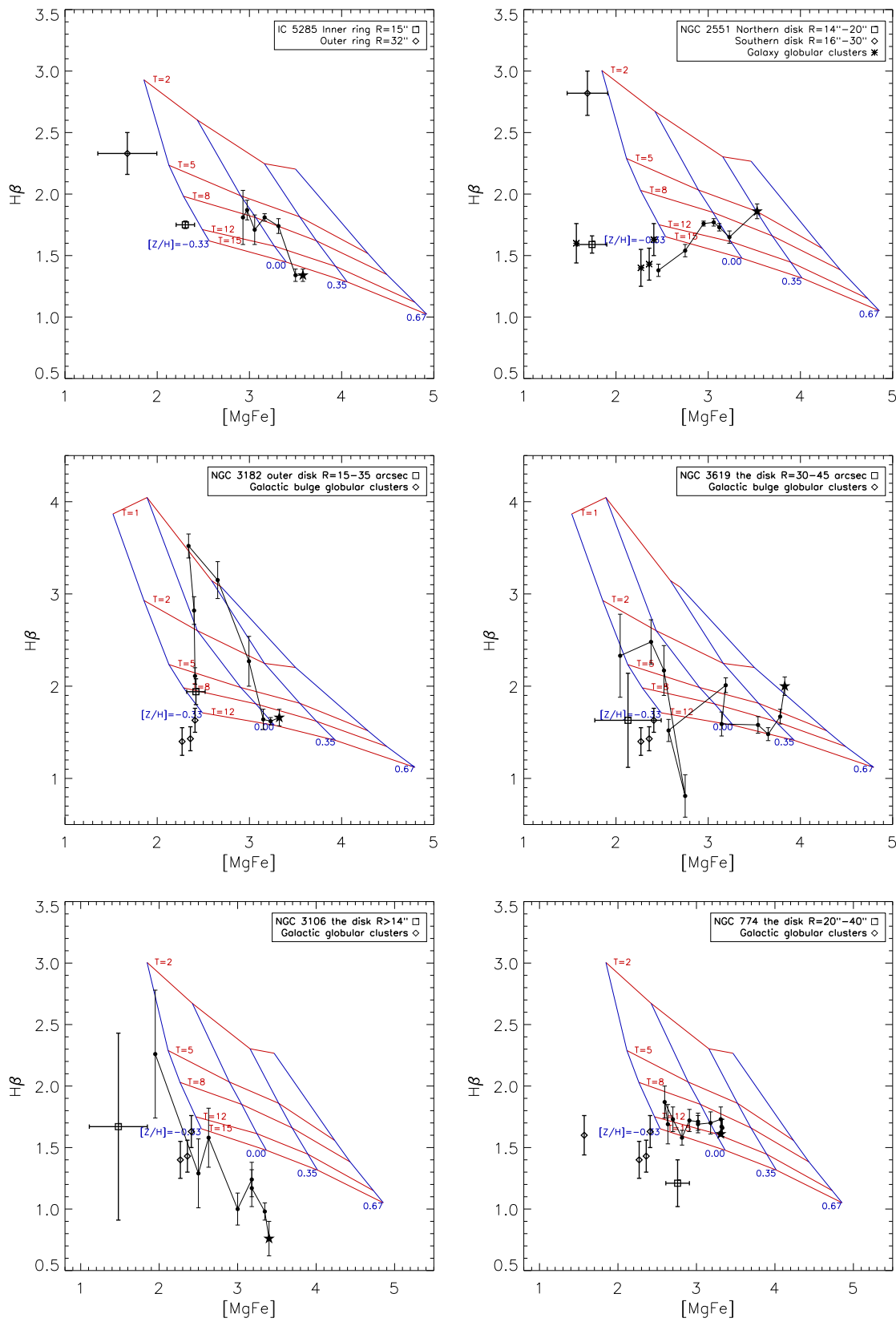


Figure 14. Index–index diagrams for six galaxies. By confronting the H β Lick index vs. a combined metallicity index involving magnesium and iron lines, we solve the metallicity–age degeneracy and determine these stellar population parameters with the SSP evolutionary synthesis models produced by Thomas et al. (2003). Five different age sequences (red lines) are plotted as a reference frame; the blue lines crossing the model age sequences mark the metallicities of +0.67, +0.35, 0.00, and -0.33 from right to left. Large black stars correspond to the nucleus for every galaxy, and then we go along the radius through the points $R = 1'', 2'', 3'', 4'', 6'', 9'', 12''$... A few globular clusters from Beasley et al. (2004) belonging to the Galactic bulge are also plotted for the reference frame.

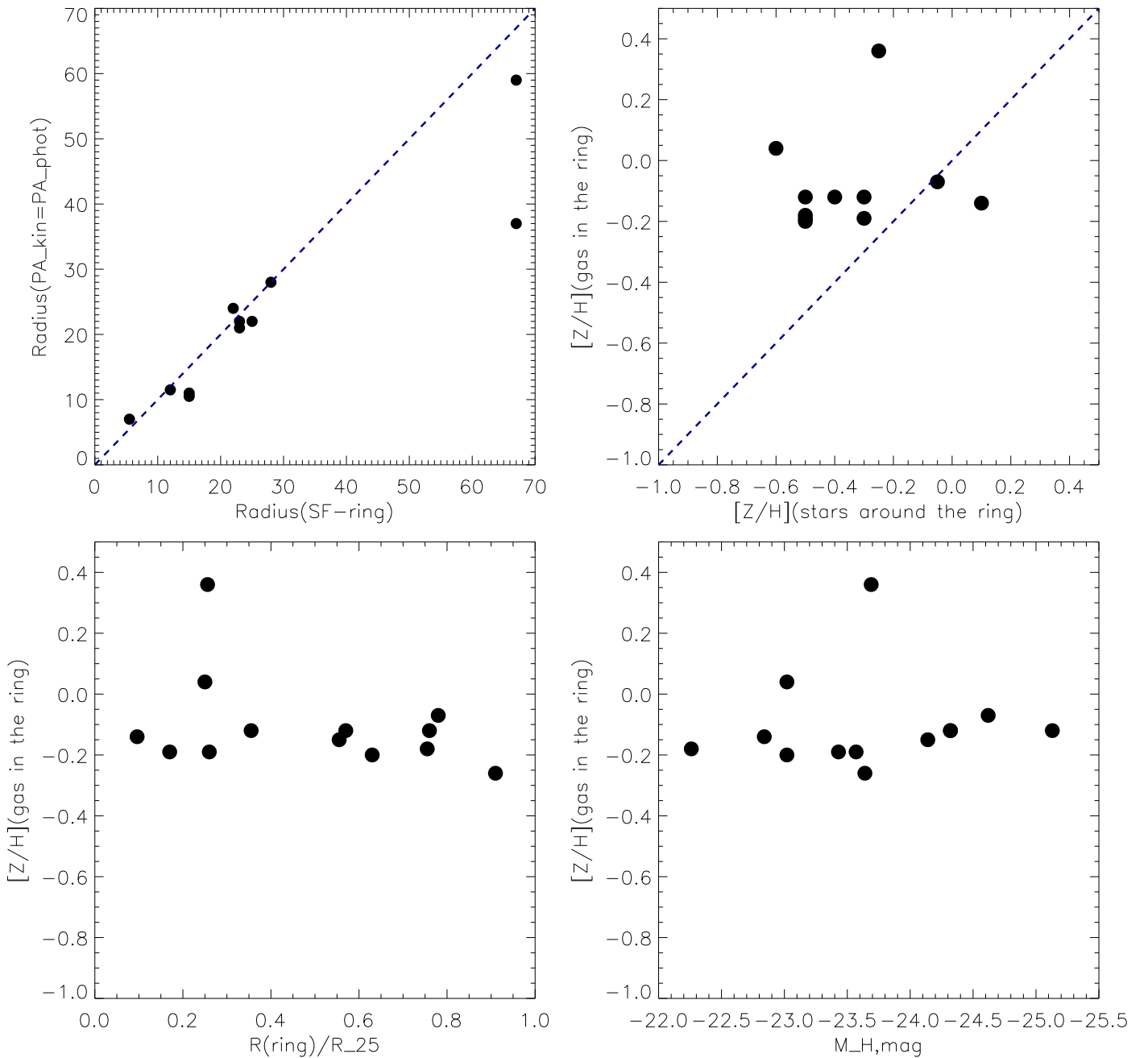


Figure 15. Some correlations for the positions and metallicities of the star-forming rings; we treat here the oxygen abundance of the gas as a measure of its total metallicity because the oxygen is the most abundant element among those heavier than the helium.

expect that the DIG contribution is significant in the studied clumps if there are nearby massive star-forming regions (like those observed in spiral galaxies, e.g., in M51; Greenawalt et al. 1998). However, the models of DIG ionized exclusively by filtered quanta do not fully reproduce the enhanced [O III] emission lines (Weber et al. 2019), while at least for NGC 3166 the ratio of [O III] $\lambda 5007/H\beta$ is clearly high in comparison with the clumps related to H II regions (see Figures 11, 12). Thus, the ionization by shocks in the clumps above the “maximum starburst line” is a preferred mechanism at least for this galaxy.

Figure 15 presents some correlations (or the absence of any correlations) related to the UV rings; for several galaxies (NGC 2697, NGC 2551, IC 5285) we take into account the multiple UV rings at various radii. The top left panel demonstrates that the radial localization of the UV-bright

star-forming rings is not casual: the radii of the rings coincide exactly with the zones where the kinematical major axes are in agreement with the lines of nodes (Figure 8), or where the gas exhibits laminar circular rotation in the main planes of the stellar galactic disks. The only point that is not close to the equality line is NGC 2962, where the outer ring is traced by our scanning Fabry–Perot only partly owing to its extreme patchiness, and the outermost radius caught by the DETKA software is $R \approx 40''$ —only two-thirds of the ring radius. From the overall statistics we can conclude that the necessary condition of the star formation triggering in a ring of S0 galaxy is gas concentration strictly in the main plane of a galaxy and laminar circular rotation within this plane. The other three plots of Figure 15 demonstrate a surprising homogeneity of the gas metallicities within the *star-forming* rings: they are all concentrated

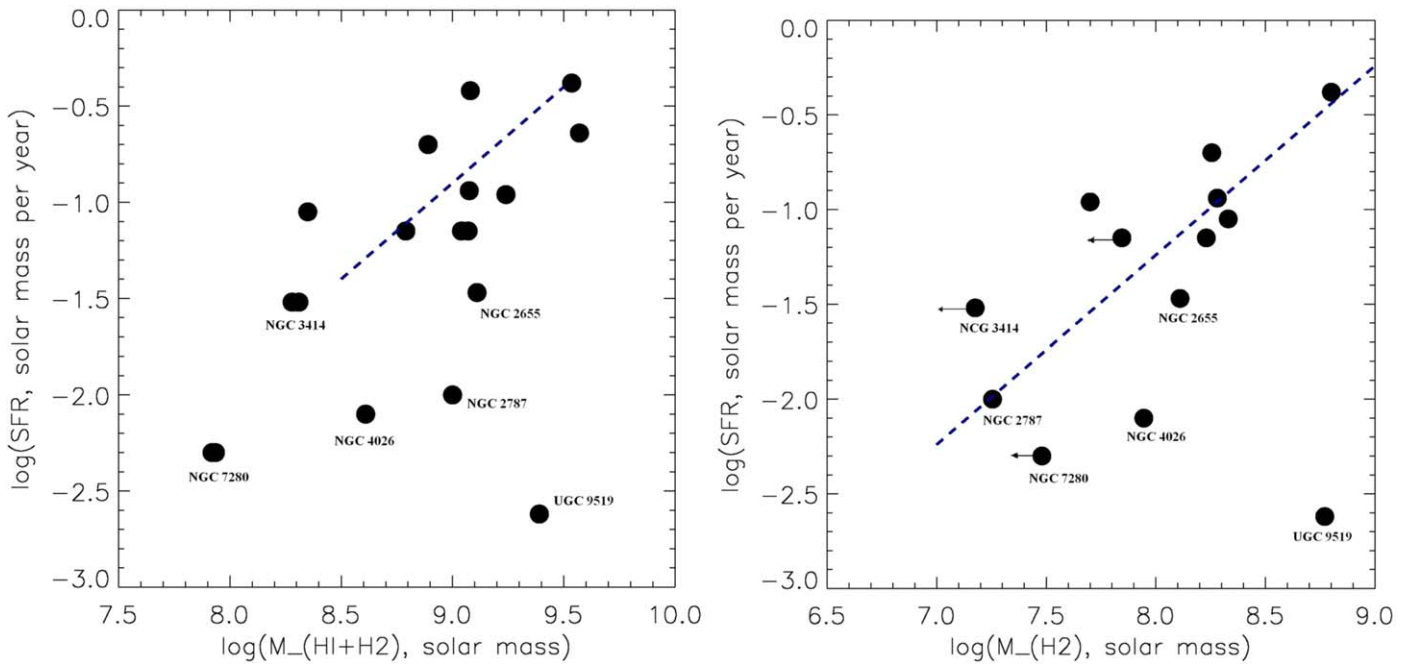


Figure 16. Correlation of the integrated SFR with the gas content of the S0 galaxies in our sample. The slope of the dashed straight line is 1. In the left plot for three galaxies with only upper limits on H_2 content we give two signs (circles) for every galaxy—one for the H_2 mass equal to the upper limit and the other for the zero H_2 mass.

around the slightly subsolar value, -0.15 dex, and correlate neither with the radius of the ring nor with the metallicity of the underlying stellar population. The stellar population metallicities have been estimated here from the Lick indices measured in our long-slit spectra by confronting them to the evolutionary synthesis models from Thomas et al. (2003). The metallicities of the stellar populations are either taken from our earlier works (Ilyina et al. 2014; Proshina et al. 2019) or calculated particularly for this analysis from the spectra obtained with SCORPIO and SCORPIO-2; for the latter galaxies we show the index–index diagrams in Figure 14. The details of the stellar population analysis are analogous to our earlier works and can be inspected in Ilyina et al. (2014). The only point with a supersolar metallicity in Figure 15 is a star-forming ring in NGC 774, which is perhaps dominated by shock-wave excitation (see the BPT analysis above, Figure 11), and for which the gas oxygen abundance estimate in Table 5 may hence be unreliable.

To illustrate once more our thesis about star formation suppression by gas accretion from highly inclined directions, we have calculated integrated star formation rates (SFRs) for our galaxies having the integrated FUV magnitudes in the NED, by using the calibrations from Lee et al. (2009), and then we have compared these SFR estimates with the total gas content in the galaxies, $H\text{I}+H_2$, compiled in our Table 1. The comparison—namely, the Kennicutt–Schmidt relation for our sample—is shown in Figure 16. One can see that most galaxies obey the Kennicutt–Schmidt relation with the logarithmic slope of 1, and this picture is consistent with the SFR confronting both the total gas mass, $H\text{I}+H_2$, and the H_2 only. But several galaxies fall below this relation, and these are the galaxies with large *polar* HI disks (see Section 5.3 and Table 6) or the galaxies where we see outer HI filaments orthogonal to the galactic planes in the HI maps by Serra et al. (2012) (see the next subsection). These galaxies may be very gas-rich, with more than $10^9 M_\odot$ of neutral hydrogen, as is observed in NGC 2655 or UGC 9519, but their current star formation is far less intense than we can expect from the Kennicutt–Schmidt relation. Interestingly, the star formation

suppression is also detected in UGC 9519 when we consider its H_2 content only. The molecular gas in UGC 9519 is confined to the central part of the galaxy, but within this central part it is also distributed in the polar plane (Alatalo et al. 2013)!

5.2. Accretion Seen “by Eye”: Neutral Hydrogen around NGC 3166, NGC 4026, and NGC 7280

NGC 3166. This galaxy is embedded into a large reservoir of HI together with NGC 3169 (to the east from NGC 3166) and NGC 3165 (to the west from NGC 3166); see Arecibo and GMRT 21 cm observations in Lee-Waddell et al. (2012). Outer streams and HI filaments coinciding sometimes with the UV-bright structures revealed by the *GALEX* survey are seen to the southeast from the galaxy. The asymmetric *inner* structure of NGC 3166 looks even more striking when we inspect the data on neutral hydrogen and on the FUV surface brightness distribution within the galaxy (Figures 13 and 17). The HI is mostly concentrated *to the east* from the nucleus (and in smaller degree in the outer western tidal arm—the only place where the ionized gas emission-line spectrum reveals excitation by young stars), while the FUV radiation is *to the west* from the nucleus. Moreover, the FUV–NUV color is extremely red to the east from the nucleus, which may be caused by asymmetric dust distribution. We cannot also exclude that the nature of the NUV radiation over this region is different from the young massive star radiation. Here it is worth mentioning that already Taniguchi et al. (1994) noted the stronger horn of the integrated CO line at receding velocities—or to the west from the nucleus, where we see now the extended strong FUV signal. In the situation in which the neutral hydrogen is localized in one half of the galaxy, and the star formation (FUV and $H\alpha$) is at the opposite side of the galaxy, where the molecular gas is also more prominent, we can only suggest a recent event of the gas acquisition, less than one orbital period ago. The whole geometry of the accretion implies a cold atomic gas infall under almost a right angle into the disk to the east from the galactic

Table 6
Mutual Inclinations of the Stellar and Gaseous Disks

| Galaxy | Stellar Disk | | Outer H I Disk | | The Angle between the Stellar and H I disks (deg) |
|----------|-------------------------|-------------------|-------------------------|-------------------|---|
| | PA(Line of Nodes) (deg) | Inclination (deg) | PA(Line of Nodes) (deg) | Inclination (deg) | |
| NGC 2655 | 110 | 20 | -60 | 60 | 80 or 40 |
| NGC 2787 | 108 | 56 | 140 | 42 | 27 or 93 |
| NGC 3414 | 12.6 | 33 | 150 | 40 | 67 or 26 |
| NGC 3619 | 63.5 | 21.5 | 73 | 30 | 10 or 51 |
| UGC 9519 | 250 | 55 | 200 | 40 | 39 or 84 |

center, where shock gas excitation dominates in the emission-line spectrum. Further gas redistribution over the whole galactic disk proceeds probably in the strongly turbulent regime, because we see the gaseous disk precession near the center (Figure 8). The gas compression along the trajectories of orbital rotation provides current formation of molecular clouds and current star formation to the west from the galactic center. Thus, the star-forming ring in NGC 3166 is still incomplete.

NGC 4026. This is another galaxy where a highly elongated HI filament that is almost perpendicular to the galaxy plane seen edge-on is observed in the wide galaxy outskirts (Serra et al. 2012). This time the gaseous stream penetrates NGC 4026 just near the center at a right angle. As a result, we see nearly polar rotation of the gas traced by the [O III] $\lambda 5007$ emission line up to $R \approx 10''$ (Figure 4). In the outer part of the galaxy, within the area dominated by the large-scale disk, the ionized gas and the neutral hydrogen are confined to the galactic plane (Figure 17) and rotate *together* with the stellar component of the disk. Interestingly, despite the rather large amount of the gas in the galaxy and its rather regular distribution and kinematics, no traces of star formation are found all over the galaxy—no H α emission lines, no FUV signal.

NGC 7280. This galaxy is quite similar to NGC 4026 in all aspects but one. Lacking current star formation and H α emission lines in the disk spectrum, it has a circumnuclear polar disk, seen both in the ionized gas kinematics (Figure 4) and in the HI distribution (Serra et al. 2012), but in the outer-disk area the gas *counterrotates* the stars. NGC 7280 is not exactly edge-on, and our surface photometry reveals some signs of triaxiality in its center (Afanasiev & Sil'chenko 2000; see also the isophote turn in Figures 8 and 17, right panels); however, the outer gas rotation looks circular, though in the opposite sense from that of the stars.

5.3. Extended Inclined Gaseous Disks: Neutral Hydrogen around NGC 2655, NGC 2787, NGC 3414, NGC 3619, and UGC 9519

NGC 2655. The galaxy was mapped in HI and analyzed in detail by Sparke et al. (2008). The outer HI distribution resembled a huge disk, with the radius exceeding the optical one by a factor of 2, and the orientation of this disk in its outer parts was strongly different from the orientation of the stellar disk. However, the HI velocity field obtained with a spatial resolution of about $40'$ (~ 3.5 kpc) looked bisymmetrical, and Sparke et al. (2008) had constructed a model of a strongly warped, circularly rotating gaseous disk produced probably by multiple minor mergers a few gigayears ago. Indeed, NGC 2655 is the center of a group, and several small gas-rich galaxies are still seen not far from it. The *multiple* mergers are needed because the total mass of neutral hydrogen in the

galaxy, $2 \times 10^9 M_{\odot}$, is too large to be provided by a single satellite sinking. Our present data, revealing a strong velocity anomaly close to the center, in some $10''$ to the north, put into doubt a relaxed character of the gas distribution in the galaxy; perhaps satellite ingestion by NGC 2655 continues just now. We see no signs of current star formation in and around NGC 2655, and this conclusion coincides with the opinion by Sparke et al. (2008).

NGC 2787. The galaxy was mapped in the 21 cm line with the WSRT by Shostak (1987). He reported an HI ring with a radius of 10 kpc, beyond the optical borders of the galaxy, with regular circular rotation implying the orientation of the line of nodes of the gaseous disk plane in $PA = 140^{\circ} \pm 5^{\circ}$. It is almost orthogonal to the inner rotation plane of the ionized gas (Figure 8) and also strongly different from the orientation of the stellar disk, $PA_0 = 108^{\circ}$. The gaseous disk isovelocity contour twist in the central part of NGC 2787 may be explained by a strong bar aligned in $PA = 160^{\circ}$; perhaps the gas when inflowing to the center is settling into a main plane of the triaxial potential orthogonally to the bar major axis. But the outer neutral hydrogen strongly decoupled from the stellar body is evidently accreted from outside, though NGC 2787 is recognized as a completely isolated S0. Again, any star formation is absent over the whole galaxy extension.

NGC 3414. An extended, regularly rotating HI disk of this peculiar S0 galaxy has been mapped by Morganti et al. (2006). Earlier the galaxy was included in the first survey with the SAURON and later classified as a slow rotator though S0 (Emsellem et al. 2007). In fact, the low projected stellar rotation of NGC 3414 is not unexpected because of the disk orientation being nearly face-on (Salo et al. 2015). However, the gaseous disk extending up to $R > 100''$ looks much more inclined to the sky plane, and so much faster rotating, up to $V_{\text{rot,proj}} > 150 \text{ km s}^{-1}$ (Morganti et al. 2006). The kinematical major axis and visible elongation of the large-scale gaseous disk is $PA_{\text{kin,H I}} \approx 140^{\circ}$ (see Figure 17), which differs from the stellar isophote major axis, $PA = 12^{\circ}$ (Salo et al. 2015), and from the thin “bar” elongation in $PA \sim 20^{\circ}$. In the very center, $R < 10''$, the gas rotation plane starts to turn, and the kinematical major axis traced by the [O III] $\lambda 5007$ emission-line velocity field aligns with the “bar” (Figure 4). In Figure 8 we have plotted the ionized gas kinematical major-axis orientation by dark-black squares (our Fabry–Perot data) and by light-black squares (SAURON [O III] $\lambda 5007$ velocity map); both data sets consistently indicate a strong turn of the kinematical major axis by $\sim 90^{\circ}$, toward $PA < 50^{\circ}$ at $R < 3''$. This “polar” velocity structure is aligned with the morphological feature in $PA \sim 20^{\circ}$, which is sometimes described as a bar and sometimes as a polar ring (Whitmore et al. 1990). Since the stellar photometric and gas kinematical major axes coincide at $R < 3''$, the data are more consistent with the hypothesis of a

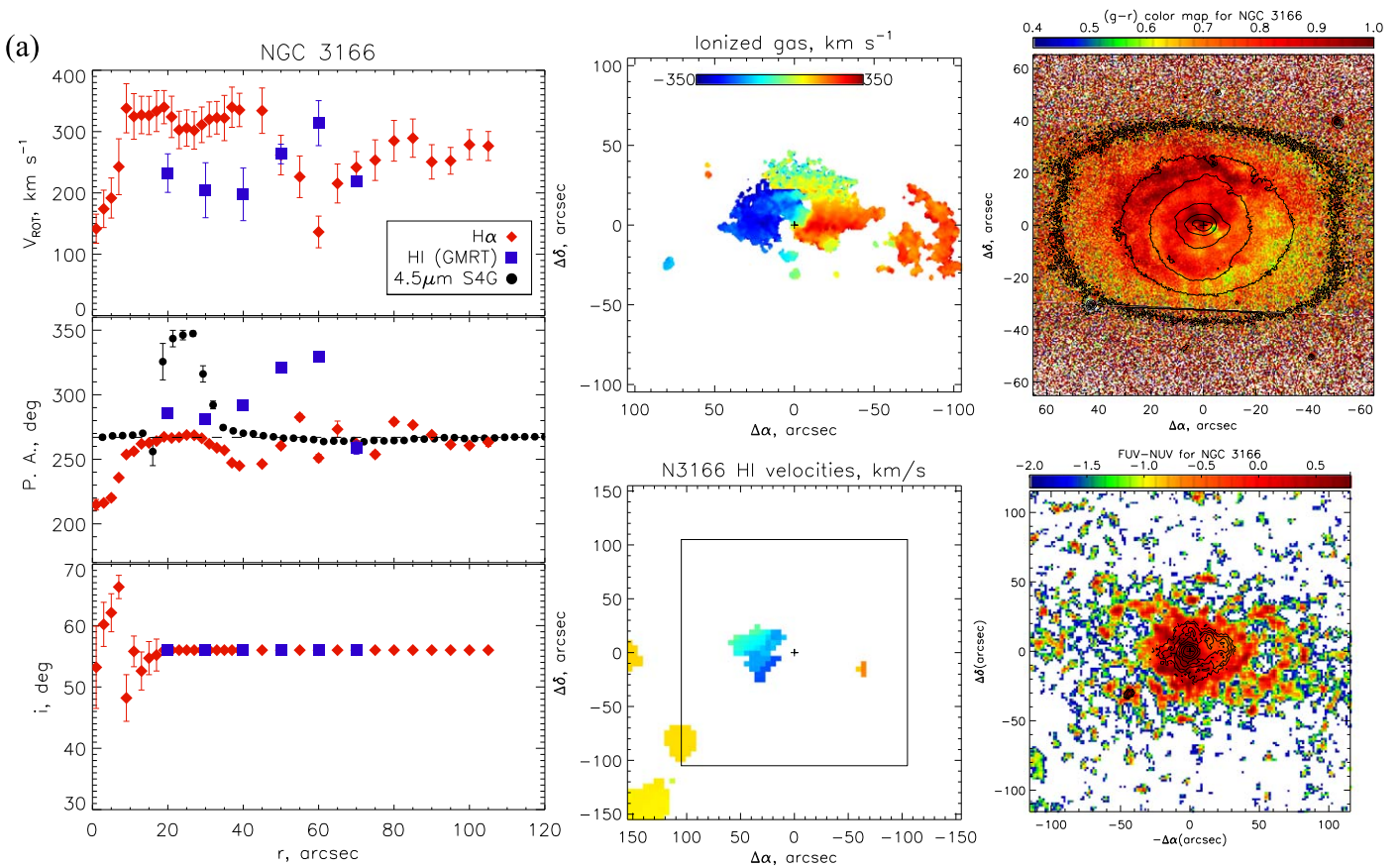


Figure 17. (a) Comparison of the ionized gas and neutral hydrogen kinematics for NGC 3166. The left panels show the radial variations of the tilted ring model parameters for the ionized and neutral gas data: the rotation velocity (top), the PA_{kin} together with PA of the NIR isophotes from S4G survey (middle), and the inclination (bottom). The ionized gas (FPI) and H I (GMRT observations from Lee-Waddell et al. 2012) velocity fields in the same color scale are shown in the middle panels. The field of view of the FPI map is marked by a square on the H I map. The velocity fields are shown after subtraction of the galaxy systemic velocity. The FUV–NUV and $g - r$ color maps are shown in the right panels. The isophotes are overlaid: the r -band ones onto the $g - r$ map and NUV ones onto the FUV–NUV map. (b) For NGC 3182 (top panels) and NGC 3414 (bottom panels). The H I maps here and below were obtained at the WSRT and originally presented in Serra et al. (2012). The original FITS were downloaded from WSRT/Atlas3D data archive (<http://wow.astron.nl/>). (c) For NGC 3619 (top panels) and NGC 4026 (bottom panels). (d) For NGC 7280 (top panels) and UGC 9519 (bottom panels).

polar disk; however, this polar disk seen strictly edge-on lacks any gas at $R > 10''$. Again, over the whole extension of the gas distribution any star formation is absent (Shapiro et al. 2010).

NGC 3619. The neutral hydrogen had been mapped in this galaxy as early as in 1989 (van Driel et al. 1989) with the WSRT. The whole gas distribution resembled an inner ring embedded into the optical body of the galaxy. The stellar velocity maps were obtained twice, in the frames of the panoramic spectral surveys ATLAS-3D (Krajnovic et al. 2011) and CALIFA (Garcia-Lorenzo et al. 2015; Sánchez et al. 2016), and we have made the tilted ring analysis of both velocity fields. The combined analysis of the stellar kinematics and surface brightness distributions retrieved from SDSS and S4G (Sheth et al. 2010) implies that the stellar disk of this galaxy is seen nearly face-on: the isophote ellipticity is approximately 0.1, which gives us the inclination of 25° under the disk relative thickness of 0.22 (Chudakova & Sil'chenko 2014), and the kinematical inclination provided by the tilted ring analysis is also $< 30^\circ$ at $R > 10''$. However, the visible cold gas rotation velocity in the inner region of the galaxy measured through the interferometric mapping of CO (Alatalo et al. 2013), H I (van Driel et al. 1989), and our $H\alpha$ data is $\sim 200 \text{ km s}^{-1}$, resulting in a kinematical inclination estimate of about 50° . The line-of-nodes position angles are also different: 85° – 90° for the gas against $PA_{0,\text{kin}} = 50^\circ$ for the stellar component (Figures 8 and

17). This means that the gaseous disk in its central part is strongly inclined with respect to the stellar disk plane; the southern part of the gaseous disk is the nearest to us because we see a red dust lane projected against the bulge at the color $g - r$ map (Figure 17). Interestingly, the UV ring at a radius of $20''$ in NGC 3619 is absolutely round, which implies that the gas compression is strictly within the plane of the stellar disk. Perhaps in the outer parts of the disk the gaseous sheet falls completely into the main plane of the galaxy—see the profiles of the left panel of Figure 17 beyond $R > 70''$.

UGC 9519. Recent deep mapping of the neutral hydrogen in UGC 9519 by M. L. Zhang et al. (2019, in preparation) has revealed the multitiered structure of cold gas distribution in this galaxy. M. L. Zhang et al. (2019, in preparation) identify three main zones of this distribution: the center, $R < 25''$, the inner ring, $R = 40''$ – $80''$, and the outer ring at $R \sim 3'$, or $> 20 \text{ kpc}$! Our Fabry–Perot data obtained in two emission lines, $H\alpha$ and $[N II] \lambda 6583$, trace the central zone, which lacks any star formation and rotates with the line of nodes in $PA \approx 150^\circ$, in polar orientation with respect to the stellar disk, and also the inner ring, up to $R \approx 80''$, rotating in a plane with the line of nodes in $PA \approx 20^\circ$; hence, our data are completely consistent with the H I orientation and rotation (Figure 17). The “inner” ring is detached from the main galactic stellar body; it demonstrates the gas excitation by young stars (our long-slit

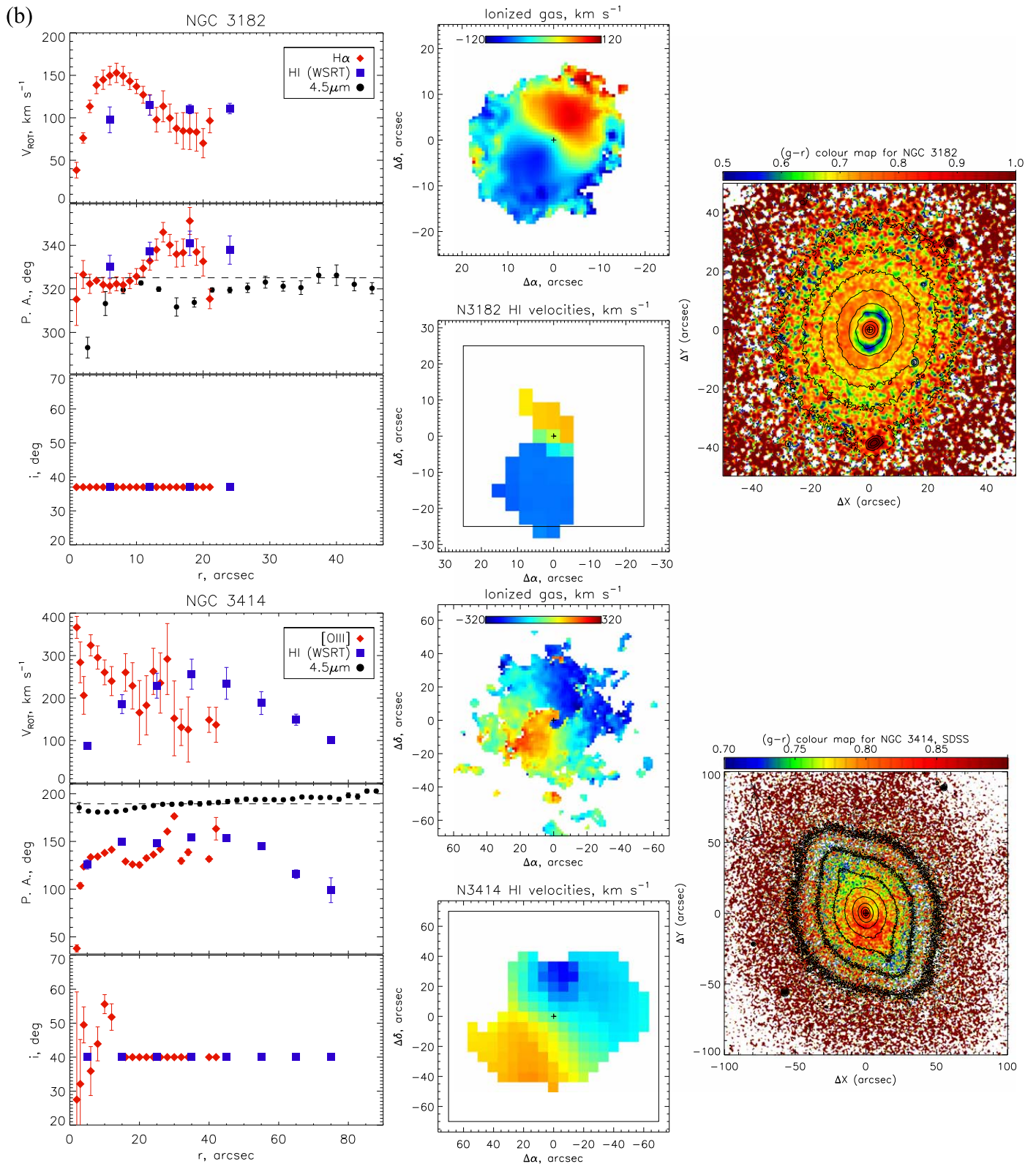


Figure 17. (Continued.)

data) and high UV surface brightness (M. L. Zhang et al. 2019, in preparation). Curiously, the molecular gas is concentrated in the central part of the galaxy (Alatalo et al. 2013), where there is no star formation; it rotates together with the ionized gas, in the polar orientation with respect to the main galactic disk.

5.4. Long-living Inclined Gaseous Disks as Treated by Dynamics

A problem of the possible steady state of inclined gaseous disks was studied more than once as a general problem of galaxy dynamics. It was provoked partly by the impressive

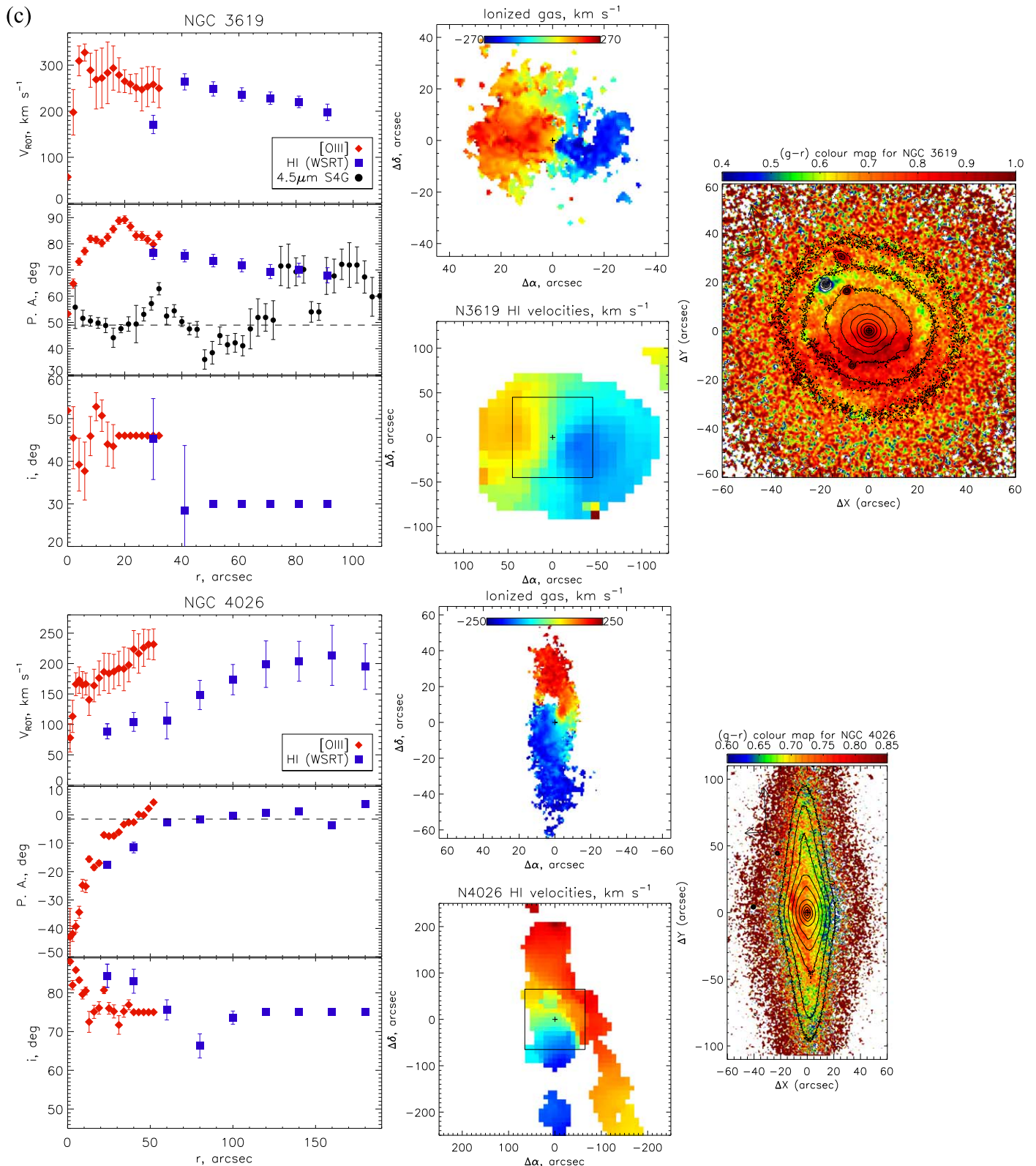


Figure 17. (Continued.)

phenomenon of large-scale polar rings, partly by understanding inevitable (common) gas accretion from an arbitrary direction. So from the 1980s to the 1990s this problem had been solved both analytically, for a case of a spheroidal potential (e.g., by Steiman-Cameron & Durisen 1988), and by numerical

simulations, for a case of triaxial tumbling potential (e.g., by Colley & Sparke 1996). It was shown that in the case of quasi-axisymmetrical potential the gas acquired under a moderate inclination—say, under 40 $^{\circ}$ —had to settle into a main galactic plane in several precession periods, which corresponded for an

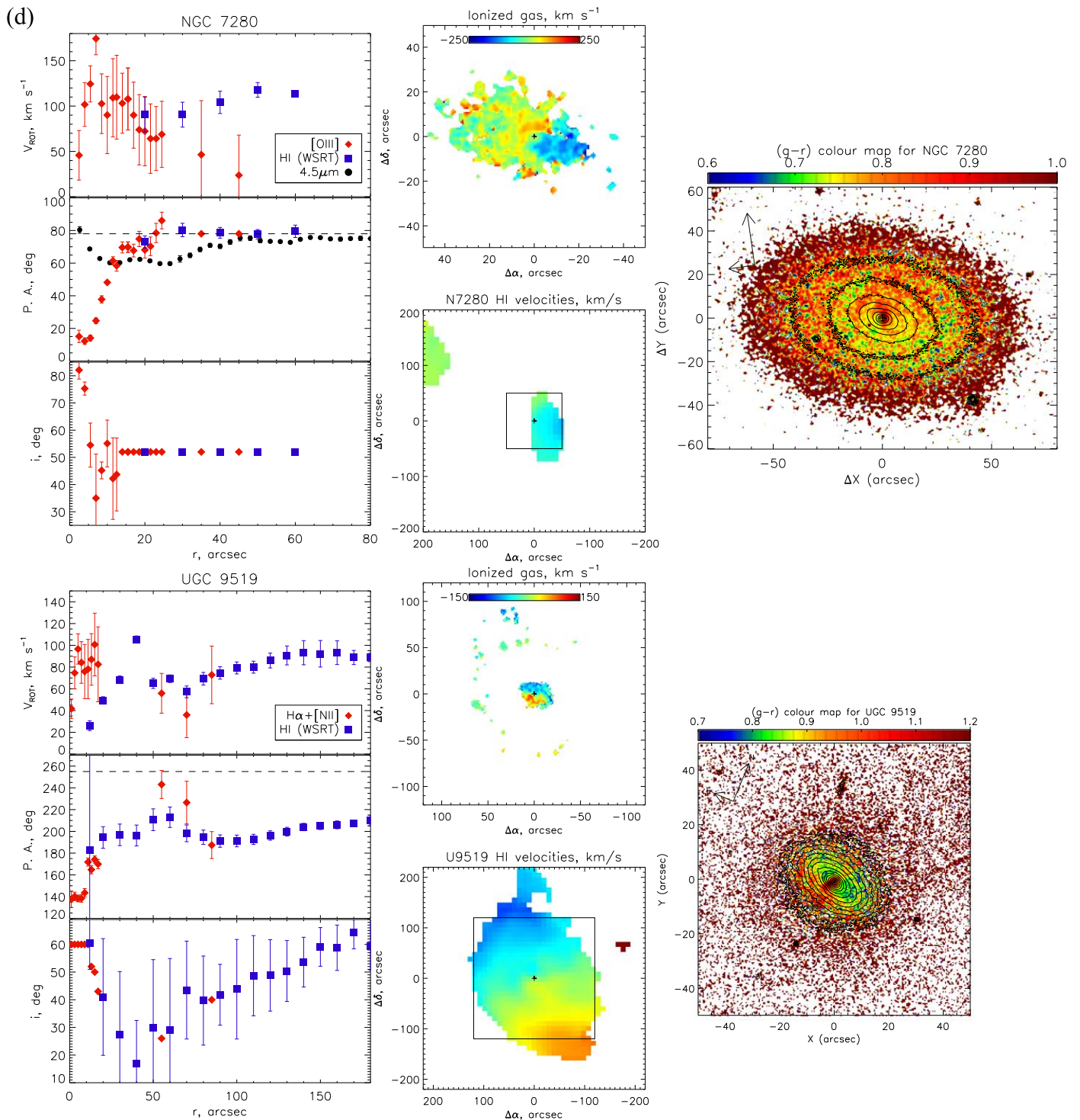


Figure 17. (Continued.)

intermediate-mass galaxy to 1 Gyr in the center, $R \sim 1$ kpc, and much longer, >6 Gyr, at $R \sim 10$ kpc (Steiman-Cameron & Durisen 1988). Christodoulou & Tohline (1993) considered *three* initial directions of gas acquisition, from under 10° , 40° , and 80° to the equatorial plane, and found significant differences in the gas behavior: the gas acquired under 10° settled into the main plane after 22–25 orbital periods, the gas acquired under 40° settled after 11–13 orbital periods, but after 8 orbital periods the disk started to suffer violent gas inflow to the center, and the gas acquired at 80° conserved its orientation

during the Hubble time but suffered also some radial inflow. Finally, within the triaxial potential the gas could settle in one of two main planes—to that orthogonal to the longest axis or to that orthogonal to the shortest axis, and the whole dynamical evolution allowed the formation of steady-state polar rings/disks (Colley & Sparke 1996).

Recently Mapelli et al. (2015) have presented the simulation of building large-scale (about 20 kpc in diameter) rings via a minor merger between a lenticular galaxy and its gas-rich satellite. The estimated living time of the ring structures has

appeared to be less than 3 Gyr if the rings form from prograde encounters, whereas it can reach 4–6 Gyr after counterrotating or non-coplanar (inclined by 45° or 90°) interactions.

In any case, the dynamical settling of an outer gaseous disk, with a radius of ~ 10 kpc, requires a very long time, so for our particular galaxies described in the previous subsection we can consider them as stationary structures, and so we can try to estimate the accretion direction by comparing the current spatial orientation of the outer HI disk with that of the stellar disk. We have made this attempt, and the results are given in Table 6. The orientations of the HI disks are taken from the papers mentioned in the previous subsection, and for NGC 3619 and UGC 9519 they are taken from our own analysis of the WSRT interferometric velocity fields. The orientations of the stellar disks are taken from the photometric decomposition results of the S4G survey (Salo et al. 2015), and for UGC 9519 we have calculated the orientation parameters of the stellar rotation plane by applying the tilted ring technique to the public SAURON data. The last column gives the estimated angles between the stellar and gaseous planes. For this calculation we have used the formula that is published by Moiseev (2012). Two values are given for every galaxy because of the uncertainty with the nearest side of any disk. Interestingly, most galaxies with steady-state extended HI disks have a possible variant of their nearly *polar* orientation with respect to the stellar disks. Only NGC 3619 has the neutral hydrogen disk with the certainly intermediate inclination; it is the smallest of all, and it contains an inner star-forming ring. Perhaps we could also note some additional consequences of the gas inflow through the inclined gaseous disks: in the galaxies with the large bars, NGC 2787 and perhaps UGC 9519, the central gas has settled into the planes orthogonal to the long axes of their *bars*.

6. Summary

We have presented the results of our spectral study of gaseous disks in 18 S0 galaxies undertaken with the facilities of the Russian 6 m telescope of the Special Astrophysical Observatory; both panoramic spectroscopy with the scanning FPI and long-slit spectroscopy over a wide spectral range with SCORPIO have been used. The gas in S0s is commonly accreted from outside, which is implied by its decoupled kinematics: at least five galaxies demonstrate extended, strongly inclined HI disks smoothly coupled with an inner ionized gas component; in three galaxies we see HI accretion directly, as thin filaments coming into the galactic disks under right angle; seven galaxies reveal circumnuclear *polar* ionized gas rotation; and in NGC 2551 the ionized gas—and neutral hydrogen too (Tang et al. 2008)—though confined to the main galactic plane, counterrotates the stellar component. The ionized gas excitation analysis at the BPT diagrams reveals the gas ionization by young massive stars in 12 of 18 S0 galaxies studied by us; the current star formation in these galaxies is confined to the ring-like zones coinciding with the UV rings seen in the galaxy images provided by the *GALEX* survey. The UV ring in NGC 774, though suffering current star formation (a Type II supernova was detected recently in this galaxy), reveals the gas excitation mostly dominated by shock waves. We have applied the tilted ring analysis to the 2D velocity fields of the ionized gas (and also of the neutral hydrogen in some objects). Tracing the orientation of the gas rotation plane lines of nodes along the radius, we have found

that current star formation proceeds usually at the radii where the gas lies in the stellar disk planes and rotates circularly; the sense of the gas rotation does not matter (NGC 2551 forms stars!). In the galaxies without current star formation the extended gaseous disks either are in a steady-state quasi-polar orientation (NGC 2655, NGC 2787, NGC 3414), or are acquired just now through the infalling highly inclined external filaments provoking probably shock-wave excitation (NGC 4026, NGC 7280). Our data imply perhaps a crucial difference of the external gas accretion regime in S0s with respect to spiral galaxies: the geometry of the gas accretion in S0s is typically off-plane.

This work is based on the spectral data obtained at the Russian 6 m telescope of the Special Astrophysical Observatory carried out under the financial support of the Ministry of Science and Higher Education of the Russian Federation. We are grateful to the staff of the Special Astrophysical Observatory and especially to Victor Afanasiev, Alexandre Burenkov, Dmitry Oparin, and Roman Uklein who performed spectral observations at the 6m telescope. We thank Michella Mapelli for her constructive comments and suggestions, which helped us to improve and clarify our results, to Karen Lee-Waddell, who has provided us with GMRT maps for NGC 3166, and to Paolo Serra, for his help with the WSRT maps. The observations in 2017 and the final analysis of the ionized gas properties have been supported by Russian Science Foundation grant No. 17-12-01335 “Ionized gas in galaxy disks and beyond the optical radius.” The analysis of star formation in the galactic rings has been supported by Russian Foundation for Basic Researches grant No. 18-02-00094a “Outer rings in disk galaxies: star formation, chemical composition, origin.” We acknowledge usage of the HyperLEDA database (<http://leda.univ-lyon1.fr>). This research has made use of the NASA/IPAC Extragalactic Database (NED), which is operated by the Jet Propulsion Laboratory, California Institute of Technology, under contract with the National Aeronautics and Space Administration. To estimate the star formation pattern in the galactic rings, we have used public archive data of the space telescope *GALEX*. The NASA *GALEX* mission data were taken from the Mikulski Archive for Space Telescopes (MAST). STScI is operated by the Association of Universities for Research in Astronomy, Inc., under NASA contract NAS5-26555. This study uses partly data provided by the Calar Alto Legacy Integral Field Area (CALIFA) survey (<http://califa.caha.es/>). The CALIFA results are based on observations collected at the Centro Astronomico Hispano Aleman (CAHA) at Calar Alto, operated jointly by the Max-Planck-Institut für Astronomie and the Instituto de Astrofísica de Andalucía (CSIC). Some figures contain the galaxy images taken from the SDSS and Pan-STARRS public databases. Funding for the SDSS-III has been provided by the Alfred P. Sloan Foundation, the Participating Institutions, the National Science Foundation, and the U.S. Department of Energy Office of Science. The SDSS-III website is <http://www.sdss3.org/>. SDSS-III is managed by the Astrophysical Research Consortium for the Participating Institutions of the SDSS-III Collaboration, including the University of Arizona, the Brazilian Participation Group, Brookhaven National Laboratory, Carnegie Mellon University, University of Florida, the French Participation Group, the German Participation Group, Harvard University, the Instituto de

Astrofísica de Canarias, the Michigan State/Notre Dame/JINA Participation Group, Johns Hopkins University, Lawrence Berkeley National Laboratory, Max Planck Institute for Astrophysics, Max Planck Institute for Extraterrestrial Physics, New Mexico State University, New York University, Ohio State University, Pennsylvania State University, University of Portsmouth, Princeton University, the Spanish Participation Group, University of Tokyo, University of Utah, Vanderbilt University, University of Virginia, University of Washington, and Yale University. The Pan-STARRS1 Surveys (PS1) and the PS1 public science archive have been made possible through contributions by the Institute for Astronomy, the University of Hawaii, the Pan-STARRS Project Office, the Max-Planck Society and its participating institutes, the Max Planck Institute for Astronomy, Heidelberg and the Max Planck Institute for Extraterrestrial Physics, Garching, Johns Hopkins University, Durham University, the University of Edinburgh, the Queen's University Belfast, the Harvard-Smithsonian Center for Astrophysics, the Las Cumbres Observatory Global Telescope Network Incorporated, the National Central University of Taiwan, the Space Telescope Science Institute, the National Aeronautics and Space Administration under grant No. NNX08AR22G issued through the Planetary Science Division of the NASA Science Mission Directorate, the National Science Foundation grant No. AST-1238877, the University of Maryland, Eotvos Lorand University (ELTE), the Los Alamos National Laboratory, and the Gordon and Betty Moore Foundation.

ORCID iDs

Olga K. Sil'chenko  <https://orcid.org/0000-0003-4946-794X>

References

- Afanasiev, V. L., & Moiseev, A. V. 2005, *AstL*, **31**, 193
 Afanasiev, V. L., & Moiseev, A. V. 2011, *BaltA*, **20**, 363
 Afanasiev, V. L., & Sil'chenko, O. K. 2000, *AJ*, **119**, 126
 Alatalo, K., Davis, T. A., Bureau, M., et al. 2013, *MNRAS*, **432**, 1796
 Andersen, D. R., Bershad, M. A., Sparke, L. S., et al. 2001, *ApJL*, **551**, L131
 Baade, W. 1975, *Evolution of Stars and Galaxies* (Cambridge, MA: MIT Press)
 Bacon, R., Copin, Y., Monnet, G., et al. 2001, *MNRAS*, **326**, 23
 Baggett, W. E., Baggett, S. M., & Anderson, K. S. J. 1998, *AJ*, **116**, 1626
 Baldwin, J. A., Phillips, M. M., & Terlevich, R. 1981, *PASP*, **93**, 5
 Beasley, M. A., Brodie, J. P., Strader, J., et al. 2004, *AJ*, **128**, 1623
 Begeman, K. G. 1989, *A&A*, **223**, 47
 Bertola, F., Buson, L. M., & Zeilinger, W. W. 1992, *ApJL*, **401**, L79
 Binette, L., Magris, C. G., Stasińska, G., & Bruzual, A. G. 1994, *A&A*, **292**, 13
 Bournaud, F., Combes, F., Jog, C. J., & Puerari, I. 2005, *A&A*, **438**, 507
 Cappellari, M. 2016, *ARA&A*, **54**, 597
 Cappellari, M., Emsellem, E., Krajnovic, D., et al. 2011, *MNRAS*, **413**, 813
 Chamaroux, P., Balkowski, C., & Fontanelli, P. 1987, *A&AS*, **69**, 263
 Chitre, A., & Jog, C. I. 2002, *A&A*, **388**, 407
 Christodoulou, D. M., & Tohline, J. E. 1993, *ApJ*, **403**, 110
 Chudakova, E. M., & Sil'chenko, O. K. 2014, *ARep*, **58**, 281
 Colley, W. N., & Sparke, L. S. 1996, *ApJ*, **471**, 748
 Cortese, L., & Hughes, T. M. 2009, *MNRAS*, **400**, 1225
 Davis, T. A., Alatalo, K., Sarzi, M., et al. 2011, *MNRAS*, **417**, 882
 Dopita, M. A., Kewley, L. J., Sutherland, R. S., & Nicholls, D. C. 2016, *Ap&SS*, **361**, 61
 Duprie, K., & Schneider, S. E. 1996, *AJ*, **112**, 937
 Eder, J., Giovanelli, R., & Haynes, M. P. 1991, *AJ*, **102**, 572
 Emsellem, E., Cappellari, M., Krajnovic, D., et al. 2007, *MNRAS*, **379**, 401
 Flores-Fajardo, N., Morisset, C., Stasińska, G., & Binette, L. 2011, *MNRAS*, **415**, 2182
 Franx, M., & de Zeeuw, P. T. 1992, *ApJL*, **392**, L47
 Garcia-Lorenzo, B., Marquez, I., Barrera-Ballesteros, J. K., et al. 2015, *A&A*, **573**, 59
 Gil de Paz, A., Boissier, S., Madore, B. F., et al. 2007, *ApJS*, **173**, 185
 Gomes, J. M., Papaderos, P., Vilchez, J. M., et al. 2016, *A&A*, **585**, 92
 Greenawalt, B., Walterbos, R. A. M., Thilker, D., & Hoopes, C. G. 1998, *ApJ*, **506**, 135
 Haynes, M. P. 1981, *AJ*, **86**, 1126
 Haynes, M. P., Giovanelli, R., Martin, A. M., et al. 2011, *AJ*, **142**, 170
 Hoopes, C. G., & Walterbos, R. A. M. 2003, *ApJ*, **586**, 902
 Hubble, E. P. 1936, *The Realm of the Nebulae* (New Haven, CT: Yale Univ. Press)
 Ilyina, M. A., Sil'chenko, O. K., & Afanasiev, V. L. 2014, *MNRAS*, **439**, 334
 Kamphuis, P., Józsa, G. I. G., Oh, S.-H., et al. 2015, *MNRAS*, **452**, 3139
 Karachentseva, V. E. 1973, *AISAO*, **8**, 3
 Katkov, I. Yu., Kniazev, A. Yu., & Sil'chenko, O. K. 2015, *AJ*, **150**, 24
 Katkov, I. Yu., Sil'chenko, O. K., & Afanasiev, V. L. 2014, *MNRAS*, **438**, 2798
 Kauffmann, G., Heckman, T. M., Tremonti, Ch., et al. 2003, *MNRAS*, **346**, 1055
 Kewley, L. J., Dopita, M. A., Sutherland, R. S., Heisler, C. A., & Trevena, J. 2001, *ApJ*, **556**, 121
 Kewley, L. J., & Ellison, S. L. 2008, *ApJ*, **681**, 1183
 Knapp, G. R., Turner, E. L., & Cunliffe, P. E. 1985, *AJ*, **90**, 454
 Koleva, M., Prugniel, P., Bouchard, A., & Wu, Y. 2009, *A&A*, **501**, 1269
 Kostyuk, I. P. 1975, *SoSAO*, **13**, 45
 Krajnovic, D., Emsellem, E., Cappellari, M., et al. 2011, *MNRAS*, **414**, 2923
 Kumari, N., Maiolino, R., Belfiore, F., & Curti, M. 2019, *MNRAS*, **485**, 367
 Lacerda, E. A. D., Cid Fernandes, R., Couto, G. S., et al. 2018, *MNRAS*, **474**, 3727
 Lang, D., Hogg, D. W., Mierle, K., Blanton, M., & Roweis, S. 2010, *AJ*, **139**, 1782
 Laurikainen, E., Salo, H., Buta, R., Knapen, J. H., & Comerón, S. 2010, *MNRAS*, **405**, 1089
 Lee, J. C., Gil de Paz, A., Tremonti, Ch., et al. 2009, *ApJ*, **706**, 599
 Lee-Waddell, K., Spekkens, K., Haynes, M. P., et al. 2012, *MNRAS*, **427**, 2314
 Lisenfeld, U., Espada, D., Verdes-Montenegro, L., et al. 2011, *A&A*, **534**, 102
 Mapelli, M., Rampazzo, R., & Marino, A. 2015, *A&A*, **575**, 16
 Marino, A., Bianchi, L., Rampazzo, R., et al. 2011, *ApJ*, **736**, 154
 Marino, R. A., Rosales-Ortega, F. F., Sánchez, S. F., Gil de Paz, A., Vilchez, J., et al. 2013, *A&A*, **559**, 114
 Mateus, A., Sodré, L., Cid Fernandes, R., et al. 2006, *MNRAS*, **370**, 721
 Moiseev, A. V. 2002, *BSAO*, **54**, 74
 Moiseev, A. V. 2012, *AstBu*, **67**, 147
 Moiseev, A. V. 2014, *AstBu*, **69**, 1
 Moiseev, A. V., & Egorov, O. V. 2008, *AstBu*, **63**, 181
 Moiseev, A. V., Valdés, J. R., & Chavushyan, V. H. 2004, *A&A*, **421**, 433
 Morganti, R., de Zeeuw, P. T., Oosterloo, T. A., et al. 2006, *MNRAS*, **371**, 157
 O'Sullivan, E., Combes, F., Salomé, P., et al. 2018, *A&A*, **618**, 126
 Odenwald, S. F. 1986, *ApJ*, **310**, 86
 Osterbrock, D. E., & Ferland, G. J. 2006, *Astrophysics of Gaseous Nebulae and Active Galactic Nuclei* (2nd ed.; Mill Valley, CA: Univ. Science Books)
 Pilyugin, L. S., & Grebel, E. K. 2016, *MNRAS*, **457**, 3678
 Poetrodjojo, H., D'Agostino, J. J., Groves, B., et al. 2019, *MNRAS*, **487**, 79
 Pogge, R. W., & Eskridge, P. B. 1993, *AJ*, **106**, 1405
 Proshina, I. S., Kniazev, A. Yu., & Sil'chenko, O. K. 2019, *AJ*, **158**, 5
 Rix, H.-W., & Zaritsky, D. 1995, *ApJ*, **447**, 82
 Roberts, M. S., Hogg, D. E., Bregman, J. N., Forman, W. R., & Jones, Ch. 1991, *ApJS*, **75**, 751
 Sage, L. J., & Welch, G. A. 2006, *ApJ*, **644**, 850
 Salo, H., Laurikainen, E., Laine, J., et al. 2015, *ApJS*, **219**, 4
 Sánchez, S. F., Garcia-Benito, R., Zibetti, S., et al. 2016, *A&A*, **594**, 36
 Sánchez, S. F., Kennicutt, R. C., Gil de Paz, A., et al. 2012, *A&A*, **538**, 8
 Sarzi, M., Falcon-Barroso, J., Davies, R. L., et al. 2006, *MNRAS*, **366**, 1151
 Schweizer, F., & Seitzer, P. 1988, *ApJ*, **328**, 88
 Serra, P., Oosterloo, T., Morganti, R., et al. 2012, *MNRAS*, **422**, 1835
 Shapиро, K. L., Falcon-Barroso, J., van de Ven, G., et al. 2010, *MNRAS*, **402**, 2140
 Sheth, K., Regan, M., Hinz, J. L., et al. 2010, *PASP*, **122**, 1397
 Shostak, G. S. 1987, *A&A*, **175**, 4
 Sil'chenko, O. K. 2005, *AstL*, **31**, 227
 Sil'chenko, O. K. 2016, *AJ*, **152**, 73
 Sil'chenko, O. K., & Afanasiev, V. L. 2004, *AJ*, **127**, 2641
 Sil'chenko, O. K., & Afanasiev, V. L. 2006, *AstL*, **32**, 534
 Sil'chenko, O. K., & Burenkov, A. N. 1990, *A&A*, **233**, 314
 Sil'chenko, O. K., Moiseev, A. V., & Afanasiev, V. L. 2009, *ApJ*, **694**, 1550

- Sil'chenko, O. K., Proshina, I. S., Shulga, A. P., & Kopusov, S. E. 2012, *MNRAS*, **427**, 790
- Simoes Lopes, R. D., Storchi-Bergmann, T., de Fatima Saraiva, M., & Martin, P. 2007, *ApJ*, **655**, 718
- Sokolowski, J., & Bland-Hawthorn, J. 1991, *PASP*, **103**, 911
- Sparke, L. S., van Moorsel, G., Erwin, P., & Wehner, E. M. H. 2008, *AJ*, **135**, 99
- Steiman-Cameron, T. Y., & Durisen, R. H. 1988, *ApJ*, **325**, 26
- Tang, Y.-W., Kuo, Ch.-Y., Lim, J., & Ho, P. T. P. 2008, *ApJ*, **679**, 1094
- Taniguchi, Y., Murayama, T., Nakai, N., Suzuki, M., & Kameya, O. 1994, *AJ*, **108**, 468
- Thomas, D., Maraston, C., & Bender, R. 2003, *MNRAS*, **339**, 897
- Ueda, J., Iono, D., Yun, M. S., et al. 2014, *ApJS*, **214**, 1
- van den Bergh, S. 2009, *ApJL*, **694**, L120
- van Driel, W., Balkowski, C., & van Woerden, H. 1989, *A&A*, **218**, 49
- van Driel, W., & van Woerden, H. 1991, *A&A*, **243**, 71
- Vauterin, P., & Dejonghe, H. 1997, *MNRAS*, **286**, 812
- Veilleux, S., & Osterbrock, D. E. 1987, *ApJS*, **63**, 295
- Weber, J. A., Pauldrach, A. W. A., & Hoffmann, T. L. 2019, *A&A*, **622**, 115
- Welch, G. A., & Sage, L. J. 2003, *ApJ*, **584**, 260
- Welch, G. A., Sage, L. J., & Young, L. M. 2010, *ApJ*, **725**, 100
- Whitmore, B. C., Lucas, R. A., McElroy, D. B., et al. 1990, *AJ*, **100**, 1489
- Wiklund, T., & Henkel, C. 1989, *A&A*, **225**, 1
- Young, L. M., Bureau, M., Davis, T. A., et al. 2011, *MNRAS*, **414**, 940
- Zhang, K., Yan, R., Bundy, K., et al. 2017, *MNRAS*, **466**, 3217